

DESIGN, ANALYSIS AND TESTING OF A
WIND TURBINE BLADE SUBSTRUCTURE

by

David Wright Combs

A thesis submitted in partial fulfillment
of the requirements for the degree

of

Master of Science

in

Mechanical Engineering

MONTANA STATE UNIVERSITY
Bozeman, Montana

March 1995

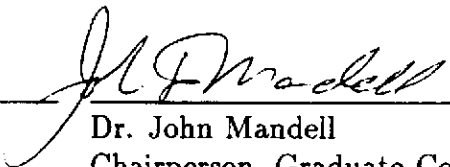
APPROVAL

of a thesis submitted by

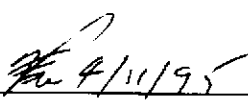
David Wright Combs

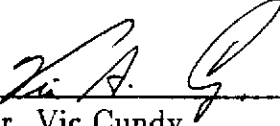
This thesis has been read by each member of the thesis committee and has been found to be satisfactory regarding content, English usage, format, citations, bibliographic style, and consistency, and is ready for submission to the College of Graduate Studies.

4/11/95
Date


Dr. John Mandell
Chairperson, Graduate Committee

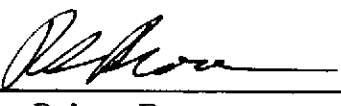
Approved for the Major Department

 4/11/95
Date


Dr. Vic Cundy
Head, Mechanical Engineering

Approved for the College of Graduate Studies

4/11/95
Date


Dr. Robert Brown
Graduate Dean

STATEMENT OF PERMISSION TO USE

In presenting this thesis in partial fulfillment of the requirements for a master's degree at Montana State University, I agree that the Library shall make it available to borrowers under rules of the Library.

If I have indicated my intention to copyright this thesis by including a copyright notice page, copying is allowable only for scholarly purposes, consistent with "fair use" as prescribed in the U.S. Copyright Law. Requests for permission for extended quotation from or reproduction of this thesis in whole or in parts may be granted only by the copyright holder.

Signature David G. Smith

Date 4-11-75

ACKNOWLEDGEMENTS

As with any project there are a variety of people without whose help this thesis would not have come to fruition.

First, thanks to Dr. John Mandell, who conceived the project, and provided insight, encouragement and prodding along the way. Thanks also to other committee members, Dr. Aleksandra Vinogradov and Dr. Michael Wells. The test fixture and numerous fabrication details were expertly handled by Gordon Williamson and Lyman Fellows. A debt of gratitude is acknowledged for Andrew Belinky, Chuck Hedley and Daniel Samborsky, members of the Materials Group at MSU who provided comradery and the all important sounding board for ideas. Dan Ruff and David Doles, undergraduate students at MSU helped to build Beams 2 and 3 and completed some of the coupon testing, for altruistic and academic reasons. The National Renewable Energy Laboratory under subcontract XF-1-11009-5 provided the funding for this project. Dr. Dan VanLuchene of the Civil Engineering Department at MSU helped tremendously in the the area of finite elements. Shawna Lockhart of the Mechanical Engineering Department helped to extract me from the AutoCAD cauldron of solid modeling.

Mary Heath, my wife, and Nathan Combs, my son, are a constant source of inspiration and support.

TABLE OF CONTENTS

	Page
LIST OF TABLES	vii
LIST OF FIGURES	viii
ABSTRACT	x
1. INTRODUCTION	1
A Brief History of Wind Turbines	1
Wind Turbines as Electrical Generators	3
Fatigue Design	5
Lifetime Analysis for Metal Structures	7
Lifetime for Composite Structures	8
Statement of Purpose	10
2. PROCEDURES	11
Coordinate Systems	11
Shape of Substructure	12
Test Configuration	12
Beam Design	12
Materials	16
Fabrication of I-Beams	17
Units	18
Orthotropic Material Properties	19
Strain Gages	19
Center Point Displacement - Beams 4 & 5	20
Coupon Tests	21
Beam Fatigue Tests	21
Finite Element Analysis	21
3. BEAM DEVELOPMENT	23
First Iteration - Configuration 1	24
Second Iteration	29

Shear Failure at the Flange Adhesive Line	34
Beam 4	36
Beam 5 - Static Test	36
4. RESULTS AND DISCUSSION	42
Overview	42
Deflection Curve Equation	42
Theoretical, FEA and Experimental Comparisons	43
Damage Development	48
Change in Stiffness	54
Strain Gage Failure	59
Failure Modes	59
Coupon Correlation	63
5. CONCLUSIONS	67
Recommendations	68
REFERENCES CITED	70
APPENDICES	73
APPENDIX A – Mold Design	74
APPENDIX B – Test Fixture	78

LIST OF TABLES

Table	Page
1 E-glass fabrics used in fabrication of I-beam.	16
2 C-channel layup schedule.	18
3 v_f for C-channels.	18
4 Lay-up schedule and v_f for flat pieces of I-beam.	18
5 Isotropic material properties for E-glass and polyester resin.	19
6 Orthotropic material properties for composite I-beam.	19
7 A summary of beam configurations and testing regime.	24
8 Test history Beam 1.	27
9 Summary of cycles and loads for beam 1.	27
10 Test history Beam 2.	27
11 Test history Beam 3.	31
12 Test history Beam 4.	40
13 Load, micro-strain and cycles summary, Beam 4. Micro-strain values are the average magnitudes of tension and compression strain measured at the initiation of each sequence.	40
14 Comparison of FEA, beam theory and experimental strain vs load slopes, Beam 2.	45
15 Comparison of FEA, beam theory and average 1 st cycle experimental displacement and micro-strain vs load slopes, Beams 4 & 5.	45
16 Ratios of predicted displacement and micro-strain slopes over average experimental slopes for Beams 4 and 5. The experimental slopes listed are those derived from the 1 st cycle of testing.	45
17 Comparison of FEA and experimental strain vs load slopes, Beam 1. .	46
18 Comparison of FEA and experimental strain vs load slopes, Beam 3. .	46
19 Comparison of FEA, theoretical and experimental displacement vs load slopes, Beams 4 & 5.	47
20 Comparison of FEA, theoretical and experimental micro-strain vs load slopes, Beams 4 & 5.	47
21 Micro-strain at failure for coupons made from flange 1 material and the compression flange of Beam 5. All geometries were tested in a static ramp loading regime.	65

LIST OF FIGURES

Figure	Page
1 Wind turbines configurations.	2
2 Configuration of original VAWT's.	3
3 Conservative estimate of fatigue cycles.	4
4 Configuration of coupon test specimens.	5
5 Fatigue design flow chart.	6
6 Laminate and beam coordinate systems.	11
7 Cross section of NREL 9.6 meter aerofoil.	12
8 Input signal from MTS control panel.	13
9 Geometric and elastic entities for composite I-beam.	15
10 Thickness variation in C-channels.	17
11 Convergence of FEA solution for Configuration 1.	22
12 Beam configurations.	25
13 Alignment of FEA coordinate system.	26
14 Pad damage Beam 1.	28
15 Compression damage zone, tension side, Beam 1.	28
16 Shear failure of adhesive line, Beam 2.	31
17 Ply drops, Configuration 3, xy plane.	32
18 Front view of tempered glass from flat plate mold with polycarbonate sheets attached for ply terminations.	32
19 Delamination of ply drops, Beam 3.	33
20 Shear damage in adhesive layer, tension flange, Beam 3.	33
21 Shear stress XY at the adhesive interface of flanges, Configuration 2.	37
22 Shear stress XY at the adhesive interface of flanges, Configuration 3.	37
23 Shear stress XZ at the adhesive interface of flanges, Configuration 2.	38
24 Shear stress XZ at the adhesive interface of flanges, Configuration 3.	38
25 Shear stress YZ at adhesive interface of flanges, Configuration 3.	39
26 FEA shear stress XY at flange interface, Configuration 2, with isotropic material properties.	39
27 Accumulated damage on inner surface of tension flange, off axis plies, 518,945 cycles, Beam 4.	50
28 Accumulated damage on inner surface of compression flange, off axis plies, 518,945 cycles, Beam 4.	50
29 Accumulated damage on inner surface of tension flange, off axis plies, 2.24 million cycles, Beam 4.	51

30	Accumulated damage on inner surface of compression flange, off axis plies, 2.24 million cycles, Beam 4.	51
31	Outer surface of tension flange, 2.26 million cycles, Beam 4.	53
32	Outer surface of compression flange, 2.26 million cycles, Beam 4. . . .	53
33	Damage in shear web of Beam 4, immediately in front of the shear web stiffener, at 2.2 million cycles.	54
34	Change in micro-strain vs cycles, Beams 3 & 4. The sharp increase in the tension micro-strain values for Beam 3 is a reflection of the growth of adhesive failure in the flange interface due to shear.	55
35	FEA and experimental strain vs load data, Beams 1 & 2.	56
36	FEA and experimental strain vs load data, Beam 3.	56
37	Piston and center point displacement vs load, Beam 4.	57
38	FEA and experimental micro-strain vs loads, Beam 4.	57
39	FEA and experimental displacement vs load results, Beam 5.	58
40	FEA and experimental strain vs load results, Beam 5.	58
41	Micro Strain and milli-volt response to strain gage failure.	60
42	Failure of Beam 1.	61
43	Failure of Beam 4.	61
44	Failure of Beam 5.	62
45	Compression failure of flange 1 coupon.	62
46	Normalized flange compressive stress with damage in shear web. . . .	63
47	Comparison of flange 1 tensile coupon results with Beam 4.	66
48	Comparison of flange 1 compressive coupon results with Beam 4. . . .	66
49	3-d and top view of plate mold.	76
50	3-d and side view of c-channel mold.	77
51	Load fixture mounted in MTS load frame with composite beam in place. .	80

ABSTRACT

This thesis presents the development of a substructure test for wind turbine blade materials (E-glass and polyester resin) and the initial experimental results obtained from this testing procedure. On going research at MSU has established baseline data for the fatigue response of rotor blade materials using coupon geometries to 10^8 stress cycles. The necessity for substructure testing is based on the accepted engineering procedure of incremental scaling towards full scale testing. In the case of composite wind turbine blades the necessity for this approach derives additional motivation due to the lack of experience with dynamic structures design for the expected lifetime of wind turbines, approaching 10^9 fatigue cycles in a 30 year service life, and the lack of experience with E-glass composite material applications at this level of cycling.

A four-point bending fixture was designed and fabricated that allowed static and fatigue testing of composite I-beams using a servo-hydraulic material testing machine. The I configuration was chosen to represent the region of the shear web and skin immediately above and below the web, of a rotor blade. Four-point bending was selected for the loading configuration due to the simplified stress state in the gage section of the beam, i.e, no shearing stress. The beams were manufactured using two resin transfer molds: one mold for the C-channels and the other for flat plates from which flanges and beam details were fabricated.

Fatigue testing of the beam pointed to the significance of structural details in fatigue design. Load and support pad failure, adhesive failure of the flange joints due to shear stress concentrations, ply-drop delaminations and shear web failure were the major developmental problems encountered. All were satisfactorily resolved except ply-drop delaminations and shear web failure. It is believed that thickening the web of the C-channels will eliminate shear web failure. Ply-drop delaminations warrant further investigation as they are commonly used in composite structures where a change in thickness is required.

The final beam design withstood over 2.2 million cycles at or above 6000 microstrain in the flanges. Of those cycles, 285,735 were at approximately 9000 microstrain. Both the static and cyclic beam flange strains at failure are close, slightly above, values predicted by coupon S-N data coupled with the finite element analysis.

CHAPTER 1

INTRODUCTION

A Brief History of Wind Turbines

Human kind has employed the wind, for both commerce and recreation, since antiquity. The inception of the windmill, or in present day terminology, wind turbine, precedes recorded history [1]. Throughout history there have been two main configurations for wind machines, horizontal and vertical axes. Fig. 1 is a conceptualization of today's horizontal axis wind turbine, HAWT, and vertical axis wind turbine, VAWT.

Vertical axis windmills appear first in historical records [1], A.D. 600-800. The rotor assembly of these machines resembled paddle wheels found on steam driven paddle boats of Sammuel Clemen's day. These machines relied upon momentum transfer or drag to produce mechanical work. In order for a moment to be created about the axis of rotation it was necessary to shield part of the rotor assembly from the wind (Fig. 2).

HAWT's, incorporating a 90° angle in the drive train appeared in the 9th-10th century [1]. This shift in axis orientation necessitated the inclusion of an oblique orientation of the blades with respect to the wind. While the designers of the day certainly did not understand the principles, aerodynamic lift was being employed, albeit rather crudely [1, 2]. This genre of windmill was prevalent in the United States, starting in the mid to late 1800's. As a testament to the basic design, it is

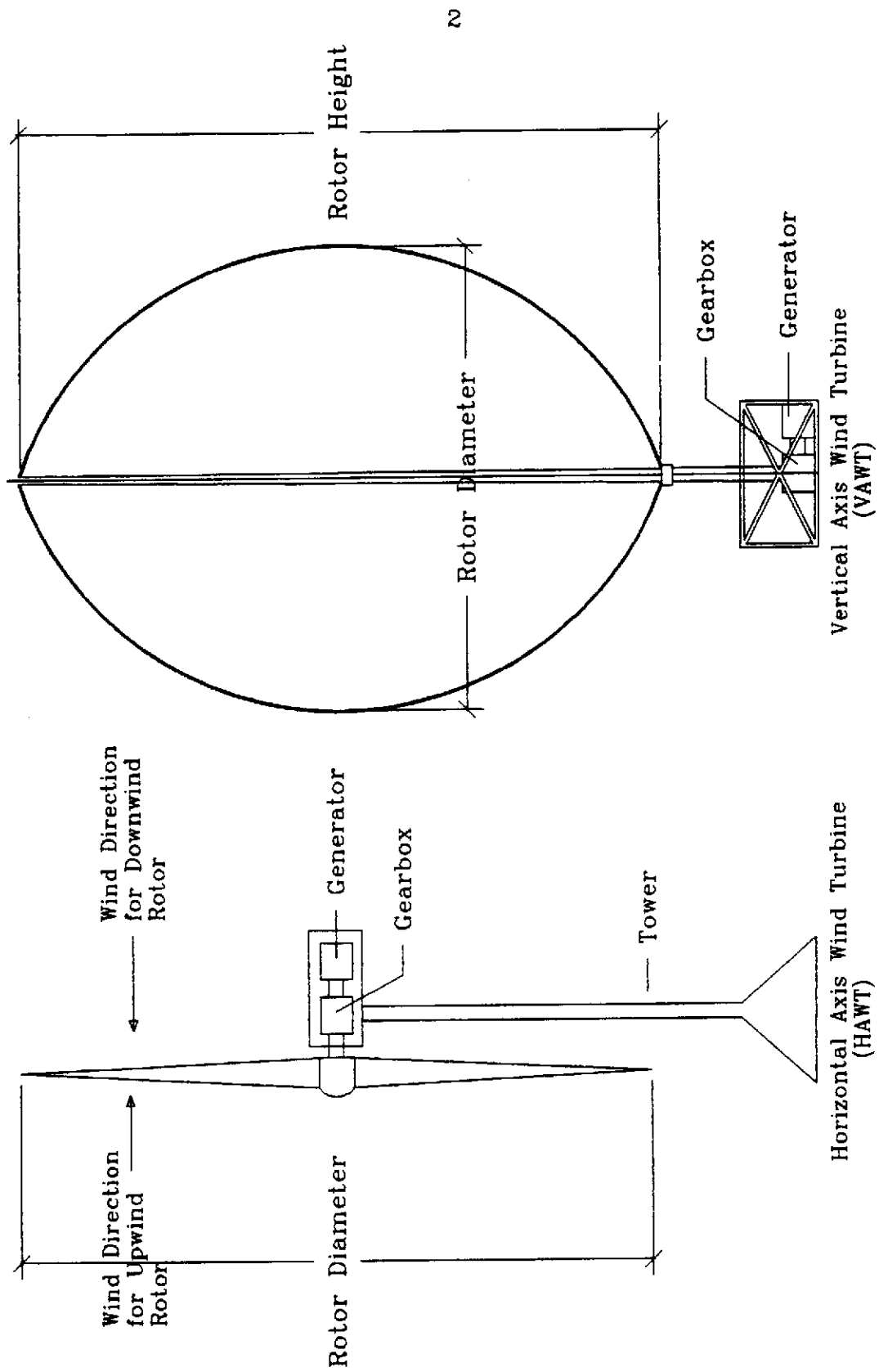


Figure 1: Wind turbine configurations.

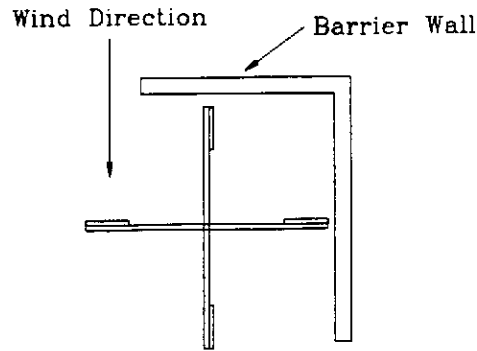


Figure 2. Configuration of original VAWT's.

estimated that there are 100,000 windmills of this variety operating in the United States today [3].

Wind Turbines as Electrical Generators

Modern wind turbines are a sophisticated synthesis of materials, aerodynamics, structural dynamics, electronic control and electrical generators. As of 1993 there were 1600 megawatts (MW) of wind energy capacity in the United States [4]. The American Wind Energy Association has set a goal of 10,000 MW of installed wind energy capacity in the United States by the year 2000 [4]. The size range of the most common wind turbines is 100-1000 kilowatts. To add perspective to these wattage numbers, at present there are approximately 16,000 wind turbines in the state of California. While California accounts for a majority of the wind turbines in the United States, wind energy is expanding throughout the United States and is a significant source of power in Europe as well.

The economic viability of wind turbines is, in part, dependent on a life expectancy of 20 to 30 years. A conservative estimate for fatigue cycles vs time for a

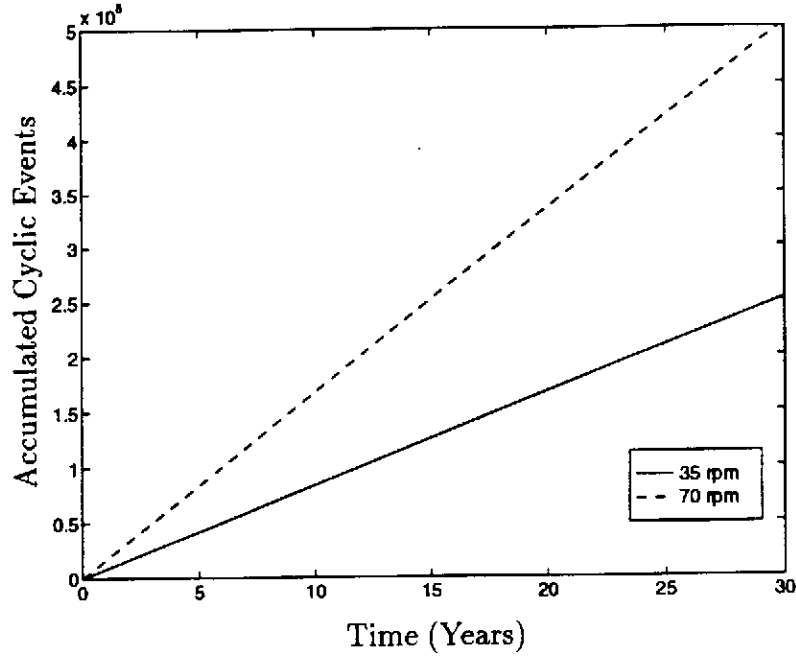


Figure 3. Conservative estimate of fatigue cycles.

wind turbine [5] is given by the equation,

$$N = 60 k \omega H_{op} t. \quad (1.2)$$

N is number of accumulated cyclic events, k is the number of cyclic events per revolution, H_{op} is the operating hours per year and t is time in years.

Fig. 3 is a plot of Equation 1.2) using $k = 1$, $H_{op} = 4000$, typical values range from 3000 to 4500 hours/year, and 35 and 70 rpm values for ω . Small wind turbines may operate at angular frequencies approaching 100 rpm while large turbine speed is approximated by 35 rpm. The use of $k = 1$ is the most conservative choice available, representing only the periodic influence of tower shadow for HAWT's. The actual loading regime experienced by a wind turbine is extremely complicated making this forecast an absolute minimum, although most cycles may experience stress amplitudes that are below levels where damage occurs in the rotor material. Wind turbines are one of the first large scale machines to be designed with a fatigue life of 10^8 to 10^9

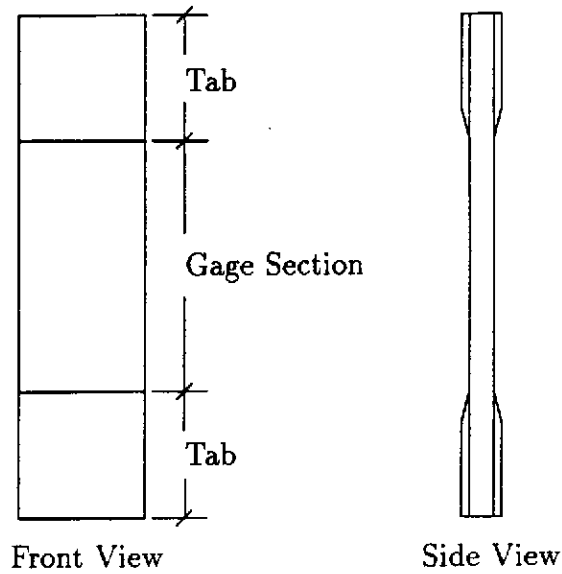


Figure 4. Configuration of coupon test specimens.

cycles [5]. Until recently, data did not exist for long term fatigue behavior of E-glass and polyester or vinyl-ester based composite materials, the material of choice in rotor blades due to the low cost. Researchers at Montana State University, Reed [6], Creed [7] and Belinky [8], have begun compiling baseline data, using coupon specimens (Fig. 4). Reed tested turbine blade material to the 10^7 decade in tension. Creed developed a high frequency test coupon that permitted testing rates of 100 Hz, which allowed 10^8 cycles to be completed in 11.6 days. Belinky established 10^8 data and testing methodology for compression at high frequency testing rates. Creed and Belinky's data are the first known long term fatigue data published for wind turbine blade materials in the United States.

Fatigue Design

Fatigue analysis and design is recognized as an essential component of the design process for any structure subjected to oscillating loads. Researchers have been

investigating the fatigue process since at least the 1800's. August Wöhler is one of the most famous fatigue researchers, conducting much of his work in the mid to late 1800's [9].

A reasonable flow chart of the design process for a fatigue sensitive structure is presented in Fig. 5. Baseline material data represents the accepted science and

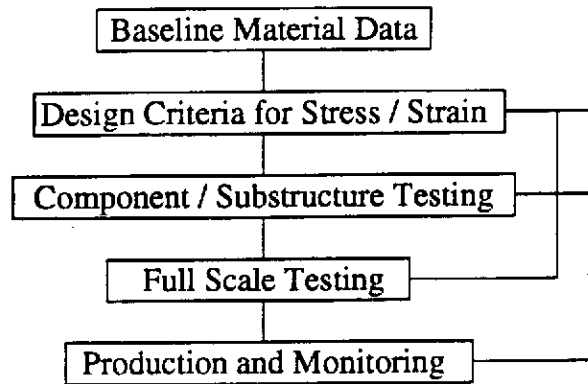


Figure 5. Fatigue design flow chart.

engineering procedure of simplifying a complicated or seemingly intractable problem in order to obtain a first approximation to the solution. The work performed by Reed, Creed and Belinky falls in this category. Design criteria for stress/strain includes an understanding of the loading regime that the device is expected to experience, component stress fields and choice of lifetime analysis methodology. Component/substructure testing, the work of this thesis, is laboratory based, controlled testing. This still employs a simplified form of the intended device, but one with sufficient complications to allow the analysis of complex geometries. Full scale testing or prototype testing may include laboratory testing and should certainly include testing in the intended use environment. Once production of the structure has begun, monitoring its response is essential in order to complete the design loop, allowing for a correlation of prediction and results and refinement of the process.

The time and financial burden required by this design procedure are not in-

significant. However, without this effort the only choice left to the designer is that of over-design, resulting in excessive weight and cost [10]. This is the environment in which wind turbines of the 1980's were designed. Premature failures of these machines in the financially conservative environment of the utilities industry evoked a warranted skepticism that was an additional hurdle for wind energy proponents to overcome.

Lifetime Analysis for Metal Structures

There are three commonly used methodologies for estimating fatigue lifetimes of metals: strain-life, stress-life and fracture mechanics [10, 11]. Stress-life is based on the work of Wöhler, i.e., applied stress vs cycles to failure plots (S-N curves), generated from specially prepared specimens (Fig. 4). Stress-life assumes elastic behavior throughout the lifetime of the material and is typically used in cases of high cycles, 10^6 for metals, and simple geometries that avoid stress concentrations. There exists a large volume of S-N baseline data for steels which makes the use of stress-life straightforward for appropriate cases.

Strain-life attempts to account for the plastic component of strain in high stress, low cycle fatigue regimes. Strain-life assumes that the volume of a laboratory test specimen accumulates damage at the same rate as the site of a stress concentration in a structure when both are subjected to the same stress/strain history [11]. The crack that fails the laboratory test specimen may not be of sufficient size to adversely affect a structure. Therefore, both the aforementioned theories are often viewed as crack initiation models.

Fracture mechanics addresses the growth of cracks and thresholds below which cracks do not propagate. Linear elastic fracture mechanics (LEFM) assumes that the stress at the crack tip can be defined in terms of the far field stress field, geometry

and a stress intensity value K . Integration of Equation 1.3 [12]

$$\frac{da}{dn} = C \Delta K^n, \quad (1.3)$$

results in a relationship between crack length and number of cycles. a is crack size, n is the number of cycles, C is a constant, $\Delta K = K_{max} - K_{min}$ and K is the stress intensity factor. Non-destructive Evaluation (NDE) techniques may be employed to establish existing flaw sizes or a flaw below the detectable limit of NDE technology is assumed to exist in critical areas. The rate of crack growth as predicted by the solution of Equation 1.3 is used as a parameter in predicting useful lifetime of a structure.

While the exact mechanisms for fatigue crack growth are not fully understood, lifetime prediction techniques have proven to be reliable in a number of cases, although no single procedure is universally accepted [9]. Metal structures that are subjected to stochastic loading regimes and whose failure could involve loss of life and/or expensive replacement are usually monitored and life prediction methodologies updated or changed in response to experience. In short, in complicated stress environments lifetime prediction of metal structures is an iterative process in response to the uncertainties of the prediction methodologies.

Lifetime for Composite Structures

Most composite materials are modeled as being elastically orthotropic or anisotropic and are inherently heterogeneous. A laminate is comprised of individual lamina, each lamina having a specific fiber orientation. The modular nature of composites allows material to be designed for specific states of stress. Fibers are aligned parallel with tensile and compressive forces or placed at 45° to yield a high shear resistance. Structural laminates will almost always contain off-axis plies to prevent brittle behavior

with respect to off-axis loadings. In the case of wind turbine material, E-glass fibers and either polyester or vinyl-ester resins, the fibers are of high strength and modulus relative to resins.

Failure mechanisms in composites are vastly different than those of metals. Damage usually initiates in the matrix of the composite due to stress concentrations at the interface of the off axis fibers and matrix [13, 14]. This damage initiates at low stress/load levels and can be a beneficial redistribution of internal stresses, i.e., stress concentrations at holes [15]. Further damage development is dispersed throughout the matrix and may initiate a limited failure of fibers and delamination of the lamina. Total separation of the material is typically associated with failure of the fibers.

The correlation of composite material baseline fatigue data, i.e., coupon data, with material response in a structure is on tenuous ground relative to metals. In large part this is due to the lack of baseline data and the complicated failure mechanisms [16]. As previously mentioned, this situation is compounded with wind turbines as a result of their high cycle lifespan.

The aircraft industry has the most experience with the application of composites in structurally critical areas. To verify lifetimes, helicopter blades are subjected to two service lifetimes of spectrum loading incorporating a load factor [16]. Fixed wing aircraft are tested in a similar manner [16]. While this procedure produces reliable components, it is far from an ideal design scenario (Fig. 5).

The present state of lifetime predictions for composite materials encourages an over-designed structure. Wind turbines are dynamic structures operating in a stochastic environment. Over-design of the blades necessitates an over-design of the entire system. For wind energy to stay on its present course of decreasing cost per kilowatt it is essential that a fundamental understanding of failure of composites be realized and lifetime prediction techniques be advanced.

Statement of Purpose

The purpose of this research was to develop a substructure representative of a wind turbine blade, as well as an apparatus for testing and test procedures that would allow fatigue testing in the laboratory at a minimum frequency of 5 Hz. A substructure being a significant structural component of present day wind turbine blades, development of such a test is the first step in correlating the results of coupon fatigue testing with material response in a rotor blade.

CHAPTER 2

PROCEDURES

Coordinate Systems

The coordinate systems used in this thesis follow convention [17, 18], with one minor exception, Fig. 6. Beam analysis typically aligns the y axis so that loads and deflections are positive. The default coordinate systems used by the computer aided design (CAD) program AutoCAD and the finite element modeling (FEM) program ANSYS were used so that loads and deflections in this thesis are negative with respect to the y axis. In laminate theory two coordinate systems are necessary. A global coordinate system, designated with x, y, z axes and a fiber direction system using 1,2,3 notation which is lamina specific. The 1 axis is parallel and the 2 and 3 axes are perpendicular to the fibers in a particular lamina.

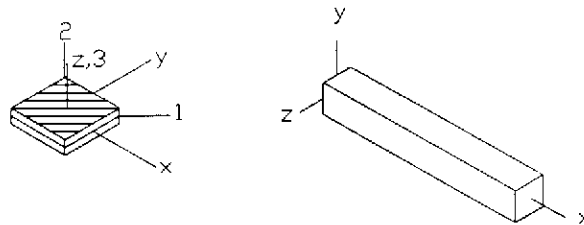


Figure 6. Laminate and beam coordinate systems.

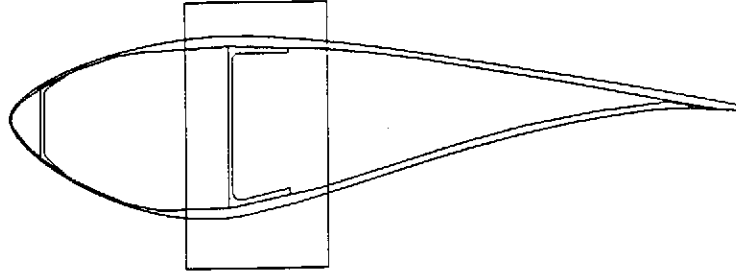


Figure 7. Cross section of NREL 9.6 meter aerofoil.

Shape of Substructure

There are three main structural designs for wind turbine blades, monocoque, d-spar and shear web. Fig. 7 is the cross-section, with structural detail, of the N.R.E.L. 9.6 meter aerofoil. The boxed area defines the structural shape, an open I, chosen for this research.

Test Configuration

HAWT blades may be modeled as cantilever beams. A cantilever beam subjected to an end load normal to the longitudinal axis experiences bending moments that vary linearly along the length of the beam, and a constant shear force. A simply supported beam subjected to four-point bending has no shear force and a constant bending moment between the two inner points of load introduction. The cantilever and four-point bending configuration were both considered for this research. Four-point bending was chosen due to the simplified stress state in the gage section of the beam.

Beam Design

A primary design consideration for the I-beam was fatigue cycle rate. A test

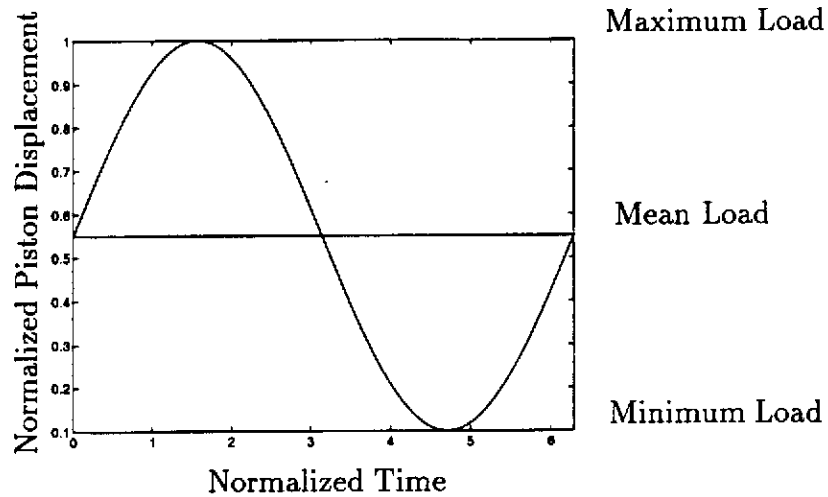


Figure 8. Input signal from MTS control panel.

conducted at 10 Hz will complete 1 million stress cycles in 27.8 hours, whereas at 5 Hz 55.6 hours is required to complete the test. Ideally, the test would be run at the highest possible rate without inducing excessive hysteresis. (Hysteresis due to cyclic loading is a measure of dissipated energy per unit volume.) With composites the heat component of this energy may induce thermal failure prior to mechanical failure [11].

The test fixture was mounted in a MTS 380.25 load frame with a servo-hydraulic valve capable of delivering 10 gallons/minute (gpm) and a force capacity of 50,000 lbs. The following equation expresses the relationship between the cubic inch/second servo-valve capacity and the limits of piston displacement (the surface area of the hydraulic piston is 19.6 inch²).

$$\frac{\text{inch}^3}{\text{sec}} = \text{area of piston} * \frac{\text{inch}}{\text{cycle}} * \frac{\text{cycles}}{\text{sec}}$$

The inch/cycle value must be divided by 4 to obtain the appropriate length value for piston movement away from the mean load (Fig. 8). A 10 Hz test rate limits piston displacement to approximately 0.050 inches. Due to the linear nature of the above equation, a 5 Hz testing rate allows for 0.10 inch movement of the piston. Piston movement is equivalent to beam displacement at the points of load introduction.

This displacement must generate sufficient strain/stress in the flange of the beam to enable a fatigue test to be completed, i.e., beam failure, in a reasonable period of time.

A beam in bending, regardless of its elastic properties, experiences strain that is proportional to the curvature and a linear function of the distance from the neutral axis [18]. Using the coordinate systems of this thesis, Fig. 6, this relationship is expressed as,

$$\epsilon = -(k * y). \quad (2.1)$$

Hookes' Law for orthotropic material in a state of plane stress and with $\sigma_y = 0$ reduces to [19]

$$\epsilon_x = \frac{\sigma_x}{E} \quad (2.2)$$

$$\epsilon_y = -\nu_{xy} \frac{\sigma_x}{E}. \quad (2.3)$$

For a laminate or a composite beam Equation 2.2 is expressed as

$$\epsilon_{xi} = \frac{\sigma_{xi}}{E_i}. \quad (2.4)$$

Substitution of Equation 2.4 into Equation 2.1 yields the expression

$$\sigma_{xi} = -(E_i k y).$$

The resultant bending moment acting on the beam is expressed as

$$M_{xx} = \int E_i k_{xx} y^2 dA. \quad (2.5)$$

Replacing the integral in Equation 2.5 with its primitive, a summation, and rearrangement yields [18],

$$k = \frac{M}{\sum_{i=1}^n E_i I_i}. \quad (2.6)$$

By viewing the shear webs and flanges of the C-channels and the outer flanges as separate and distinct geometric and elastic entities (Fig. 9) a composite flexural

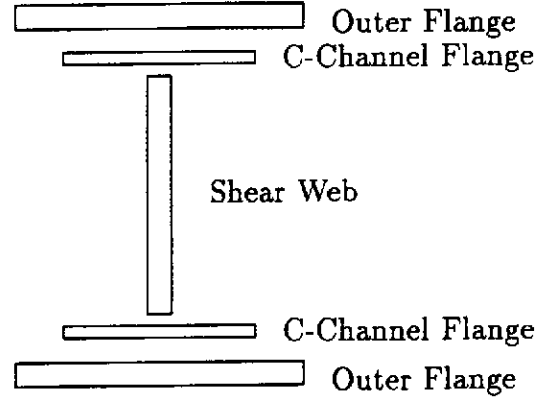


Figure 9. Geometric and elastic entities for composite I-beam.

rigidity (EI) may be calculated for any given cross-section. Employing Equation 2.6, it is then possible to calculate k_{xx} and consequently the strain at any given point in the cross-section of the I beam. For a 3 inch by 2.8 inch cross-section, flange thickness of 0.17 inches and a 24 inch length, Equation 2.6 and the deflection equation for four-point bending of a beam at the inner points of load introduction [18],

$$v(a) = \frac{Pa^2}{6EI}(3L - 4a), \quad (2.7)$$

predict that a load of 15,000 lbf will result in a deflection at the load points of 0.1678 inches and 5800 micro-strain at the center of the beam on the flange surface. The deflection levels would limit the test to approximately 5 Hz. Based on coupon fatigue data 6000 micro-strain was selected as an initial testing range.

The predictions considered thus far do not include shear deformation. The length/height ratio for the selected geometry is 8, indicating significant shear influence. The average shear stress in the web of a beam is given by [18]

$$\tau_{avg} = \frac{V}{th},$$

where V is the shear force, t is the thickness of shear web and h is the height of shear web. The average shear stress due to the above load is approximately 27,000 psi, a

Fabric	Hexcel Description	Weight (g/in^2)
Unidirectional	D155-50.0	0.380
± 45	DB240-50.0	0.558
Fabric	Fibre-Glast Description	Weight (g/in^2)
0/90 (Woven Roving)	223	0.3975
Chopped Random Mat	248	0.1177

Table 1. E-glass fabrics used in fabrication of I-beam.

stress level that would fail the web without shear web reinforcement.

Steel construction employs web stiffeners when flange shear stress levels exceed design criteria [20]. The use of structural adhesives in joining composite materials influenced the design solution for excessive shear stress due to the large surface area available for bonding (Chapter 3, Fig. 12). The compound angle of the stiffener, similar to the beveling of tabs on standard material test coupons, was chosen to reduce stress concentrations. Finite element results of this configuration showed a significant reduction in shear stress levels in the web and desirable deflection and stress/strain characteristics, as discussed in Chapter 4.

Materials

The materials used in this study are the same as those used in most wind turbine blades. CoRezyen 63-AX-051, an unsaturated orthophalic polyester resin was used exclusively. The catalyst was methyl ethyl ketone peroxide (MEKP), 2% by volume. The fabrics used were all comprised of E-glass fibers, Table 1. The unidirectional and ± 45 cloth is held in sheet form by extensive stitching. Refer to Appendix A for drawings of the resin transfer molds.

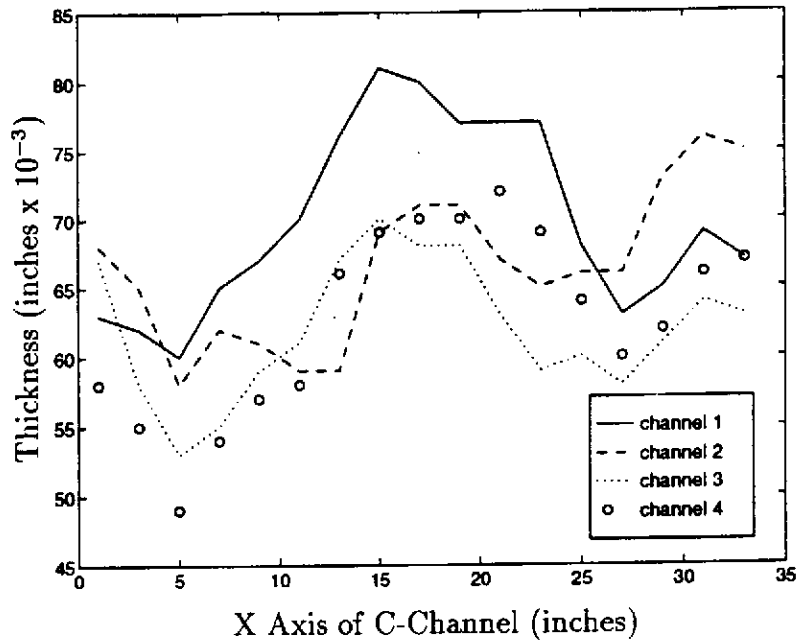


Figure 10. Thickness variation in C-channels.

Fabrication of I-Beams

Construction of the beam required the use of a high strength epoxy adhesive. Hysol EA 9309.2NA was chosen for its high shear strength. Hysol EA9412, a low viscosity epoxy, proved to be excellent in repair.

Initial manufacturing of parts yielded inconsistent thickness and consequently varying fiber volume fractions, v_f , of the composite. Injection of excess amounts of resin which induced mold deflection was determined to be the cause of this variation [21]. Once this was corrected, thickness of the parts was consistent (Fig. 10). C-channels were constructed in such a manner that each channel was of symmetric layup and when bonded together the resulting web was symmetric, Table 2. Load and support pads, shear stiffeners and flanges were made from sheet material. Parts that required thicknesses greater than that of the flat plate mold, 0.17 inch, were built-up by bonding pieces together using Hysol EA 9309.2NA epoxy adhesive, Table

Channel	Layup
#1	$(\pm 45)_s$
#2	$(\mp 45)_s$
web of I-beam	$[(\pm 45)_2]_s$

Table 2. C-channel layup schedule.

C-channel Section	v_f
Web	0.45
Flange	0.38

Table 3. v_f for C-channels.

Part	Lay-up	v_f	% 0's
Pads	$[(0/90)_4]_s$	0.45	50
Shear Stiffener	$[(\pm 45)_3]_s$	0.47	0
Flange 1	$[(\pm 45)/(0)_3]_s$	0.48	67
Flange 2			
outer section	$[c.m./(0)_2/(\pm 45)/(0)_4]$	0.42	77
gage section	$[c.m./(0)_2/(\pm 45)/(0)_2]$	0.41	69

Table 4. Lay-up schedule and v_f for flat pieces of I-beam.

4. All bonding surfaces were well sanded and cleaned with methanol before adhesive was applied. Parts were well clamped to ensure even clamping pressure and consistent bond thickness.

Units

English units, e.g. pound force (lbf) and inches are used. Micro-strain ($\mu\epsilon$) is engineering strain times 10^6 .

	Young's Modulus (psi)	Poisson's Ratio
E-glass	10^7	0.2
polyester resin	5.5×10^5	0.35

Table 5. Isotropic material properties for E-glass and polyester resin.

	Flange 1	Flange 2		C-channel		Shear stiffener
		outer	gage	flange	web	
E_x (psi x 10^6)	3.6	3.6	3.1	1.8	1.8	1.8
E_y (psi x 10^6)	1.3	1.3	1.4	1.8	1.8	1.8
E_z (psi x 10^6)	1.3	1.3	1.4	1.2	1.2	1.2
ν_{xy}	0.322	0.322	0.387	0.582	0.582	0.582
ν_{yz}	0.25	0.25	0.25	0.25	0.25	0.25
ν_{xz}	0.25	0.25	0.25	0.25	0.25	0.25
G_{xy} (psi x 10^6)	0.52	0.52	0.67	1.4	1.4	1.4
G_{yz} (psi x 10^6)	0.55	0.55	0.55	0.55	0.55	0.55
G_{xz} (psi x 10^6)	0.55	0.55	0.55	0.55	0.55	0.55

Table 6. Orthotropic material properties for composite I-beam.

Orthotropic Material Properties

E_x moduli were measured in the laboratory using an extensometer for flange 1, both cross-sections of flange 2 and the shear stiffener material. The web of the C-channel is approximately the same material as that of the shear stiffener (Tables 3- 4), therefore these volumes have the same material properties. E_y , ν_{xy} and G_{xy} were derived using laminate theory. ν_{yz} and ν_{xz} were approximated using Poisson's ratio for E glass and polyester resin, Table 5. G_{yz} and G_{xz} were approximated by the shear modulus of the resin, Table 6.

Strain Gages

Strain gages used were type WK-XX-250AF-350, single element, manufactured

by Micro-Measurements, Raleigh, North Carolina. These gages were chosen due to a large gage surface area which averages out local inconsistencies of the composite, a strain limit of 1.5% at room temperature and 350 ohms resistance to mitigate the poor thermal conductivity of composites. Micro-Measurements M-Bond AE-10 epoxy was used exclusively for bonding gages.

Strain gages were located on the tension and compression flange, outer surface, mid-span and centered laterally. Strain conditioning cards were configured as quarter bridges.

Center Point Displacement - Beams 4 & 5

Data collected from Beams 4 and 5 included displacement data taken from the center of the beam and piston displacement which should correlate closely with displacement of the beam at the load points. Center displacement measurements involved attaching a light weight aluminum bar to the compression flange with C-clamps. The bar was oriented perpendicular to the x axis of the beam. The C-clamps were tightened only to the extent necessary to ensure a firm connection. Strain output was recorded at this point, with no load applied to the beam, and never exceeded 10 micro-strain on the compression flange. The tension flange gage did not show any significant variation from calibrated zero due to the application of the bar. Dial indicators were placed using magnetic stands attached to the upper/stationary test fixture, the stem of the dial indicator contacting the aluminum bar. The beams were then loaded incrementally through the desired range, displacement and strain data were recorded. Next, the beams were unloaded to 1,000 lbf, the bar removed and strain and piston displacement was re-recorded. Center point displacement was recorded for Beam 5 only up to 12,000 lbf/10,000 $\mu\epsilon$ to avoid damaging the dial indicators. The strain data presented in Chapter 3 is that recorded without the

bar attached to the beam, as at lower loads the bar did significantly affect strain measurements on the compression flange.

Coupon Tests

Coupon S/N data were generated using Flange 1 material. Tension coupons were 8 inches by 1 inch with a gage length of 4 inches. Compression coupons measured 4.75 inches by 1 inch and gage length was 0.75 inches. All test were conducted at 15-20 Hertz. (Beams were tested in the 5-10 Hertz range, eliminating frequency effect concerns from hysteresis heating [7, 8].)

Beam Fatigue Tests

Beam fatigue tests were conducted in load control with $R = 10$, where $R = \text{force}_{\min} / \text{force}_{\max}$. Slopes from experimental strain and displacement vs load data were derived using a least squares fit of the data, forced through the origin.

Finite Element Analysis

The commercial finite element program ANSYS was used for all FEA analysis. Solutions were executed on an IBM RS 6000 resident at Montana State University and on a CRAY Y-MP resident at the National Center for Supercomputing Applications, University of Illinois at Urbana-Champaign.

The ANSYS element selected for analysis was Solid45, a 3 dimensional curved sided brick or isoparametric hexahedra. Solid45 was chosen for its 3-D and orthotropic modeling capabilities and reduced model size relative to other 3-D ANSYS elements. Models were run with element planar dimension set for 0.5. Convergence of FEA results was verified with runs on the CRAY Y-MP with a planar dimension of 0.25 (Fig. 11).

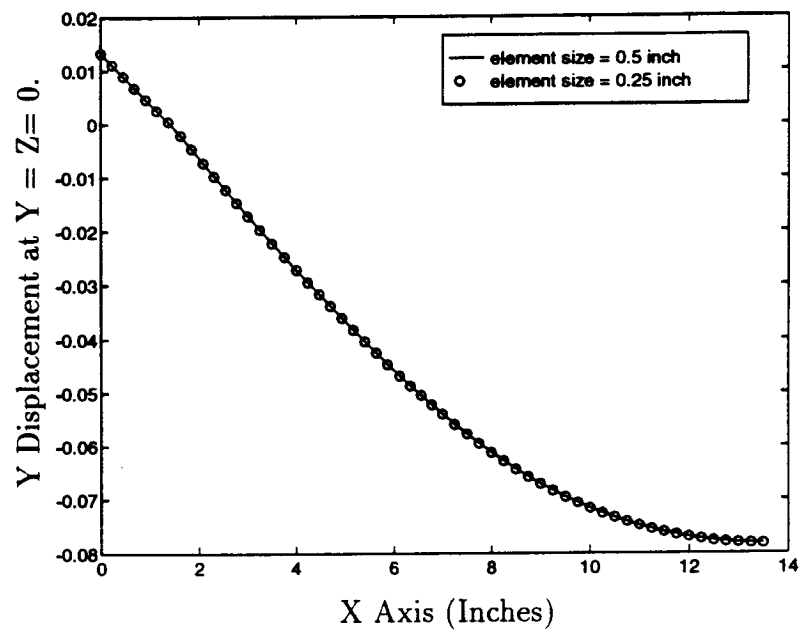


Figure 11. Convergence of FEA solution for Configuration 1.

CHAPTER 3

BEAM DEVELOPMENT

Design is necessarily an iterative process and the work of this thesis was not exempt from this axiom. Three design iterations were performed. Problems encountered included: load pad failures at the points of support and load application, shear failure of the adhesive joint between the outer tension flange and the flanges of the C-channels, and shear failure of the web. Introduction of ply drops to the flanges resulted in delaminations originating at the sites of the ply terminations.

Initial design considerations focused on the response of the beam in the gage section, i.e, the middle of the beam. As testing proceeded, the author gained additional appreciation for the attention to design detail at points of load introduction. These are the sites most likely to fail, yet were of limited experimental interest. In order to test the gage section of the beam it was essential to design smooth stress transition areas throughout the beam. Structural design that absorbs applied load as evenly distributed stress fields is successful design.

Five beams in three configurations (Fig.12), were fabricated and tested as part of this research. Table 7 summarizes differences and lists the testing schedule. Two shapes of shear stiffeners were used, shear stiffener 1, previously described, was used on Configurations 1-2, Beams 1-3. Shear stiffener 2 (Fig.12), which was symmetric with respect to the xz plane of the beam, was used on Beams 4-5. (The rationale for stiffener 2 follows in this chapter.) Using conventional beam terminology, the outside load points are referred to as supports and the inside load points are referred to as load points/pads. Fig. 13 identifies the orientation of the beam coordinate system.

Configuration	Beam Number	X-Section (Inches)	Characteristics	Test Regime
1	1 & 2	3x3	stiffener 1	fatigue
2	3	2x3	stiffener 1 ply drops	fatigue
3	4 & 5	2x3	stiffener 2 ply drops	
	4			fatigue
	5			static

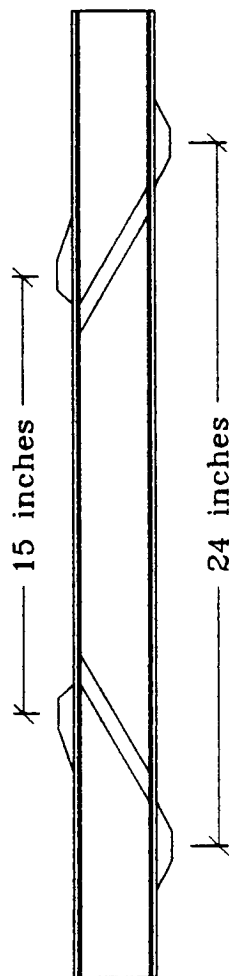
Table 7. A summary of beam configurations and testing regime.

Note that the FEA incorporated two planes of beam symmetry, therefore one quarter of the beam was modeled. The yz plane of symmetry divides the beam in half axially and the xy plane of symmetry divides the beam in half laterally.

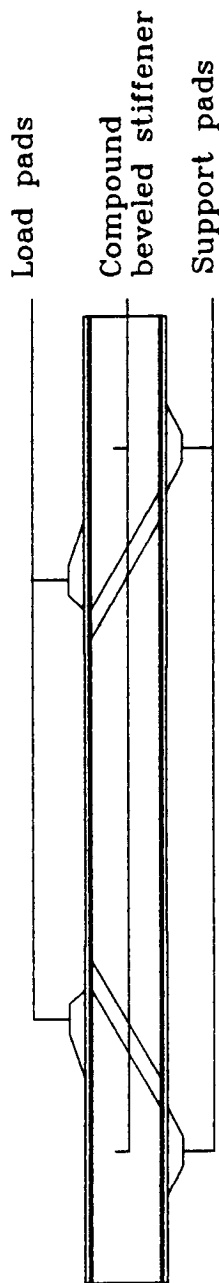
First Iteration - Configuration 1

Beam 1, the first beam tested in fatigue, was a shakedown for both beam design and the test fixture. Beam 1 pad failure (Fig. 14) was largely attributable to a design compromise of the test fixture (Appendix B). Fixture design called for roller supports for the load fixture and fixed semi-circular outer supports. The dynamics at the interface of a roller and pad are those of slip and roll whereas at the interface of a fixed support and pad is pure slip. The effects of pure slip were catastrophic to the support pads. With the addition of outside rollers, support pad failure was eliminated until 10^6 cycles were surpassed (Beam 4). Pad failure that occurred at 130,224 total cycles for Beam 1 also caused in a compression damage zone directly under one of the support pads (Fig. 15), in the region of the C-channel fillet. It is probable that insufficient control of the MTS hydraulics resulted in an overload condition, resulting in this damage. Test histories for Beams 1-2 are found in Tables 8-10.

Configuration 1
2.8 x 3 inch cross section at mid-span



Configuration 2
2.76 x 2 inch cross section at mid-span



Configuration 3
2.76 x 2 inch cross section at mid-span

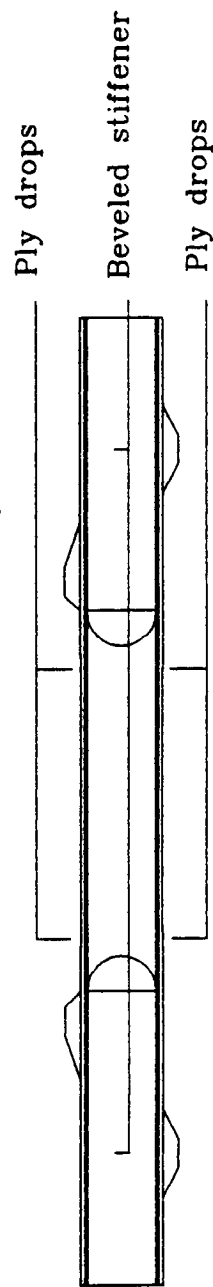


Figure 12: Beam configurations.

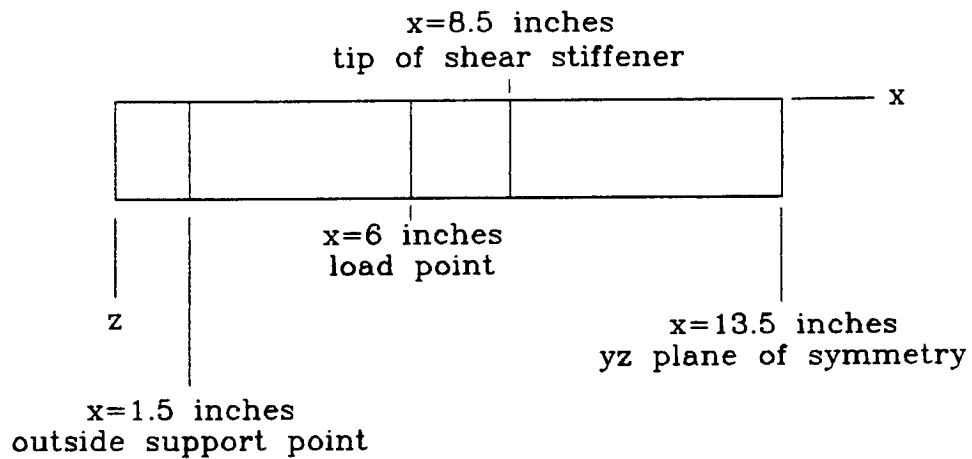
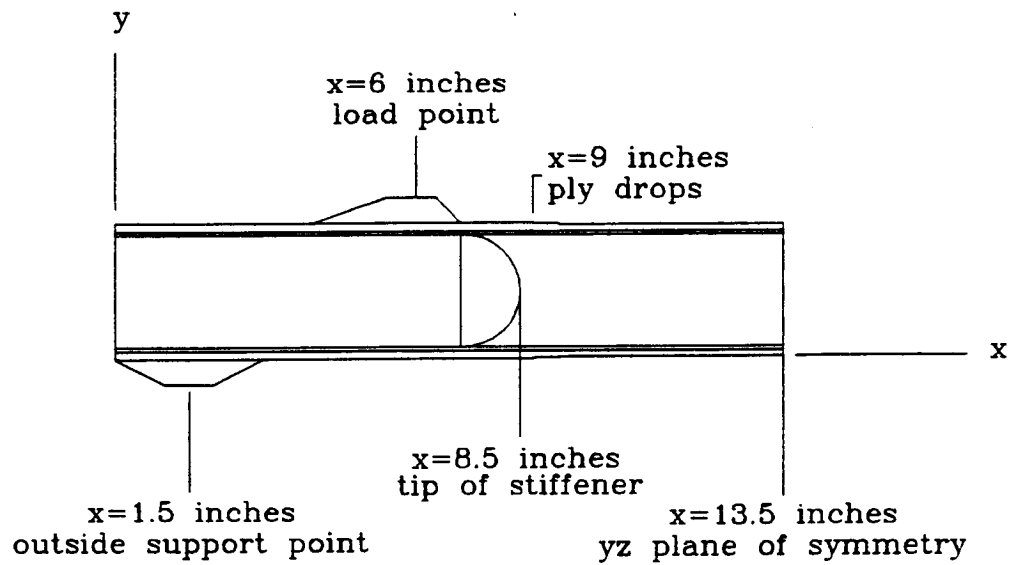


Figure 13: Alignment of FEA coordinate system. Top drawing is side view and bottom is plan view.

Total Cycles	Cycles (Sequence)	Maximum Load (lbf)	Event
1-100,000	100,000	5,000	Data
100,000-130,244	30,244	10,000	Pad Failure
130,244-189,533	59,289	10,000	Pad Failure
189,533-199,533	10,000	5,000	
199,503-207,030	7,497	10,000	Pad Failure
			Outside Rollers
207,030-217,030	5,000	5,000	Data
217,030-227,030	10,000	10,000	
227,030-256,499	29,469	15,000	Failure

Table 8. Test history Beam 1.

Maximum Load (lbf)	Total Cycles
5,000	120,000
10,000	107,030
15,000	46,419

Table 9. Summary of cycles and loads for beam 1.

Total Cycles	Cycles (Sequence)	Maximum Load (lbf)	Event
1	1		Data
1-10,000	10,000	5,000	
10,000-20,000	10,000	10,000	
20,000-36,950	16,950	15,000	Stopped

Table 10. Test history Beam 2.

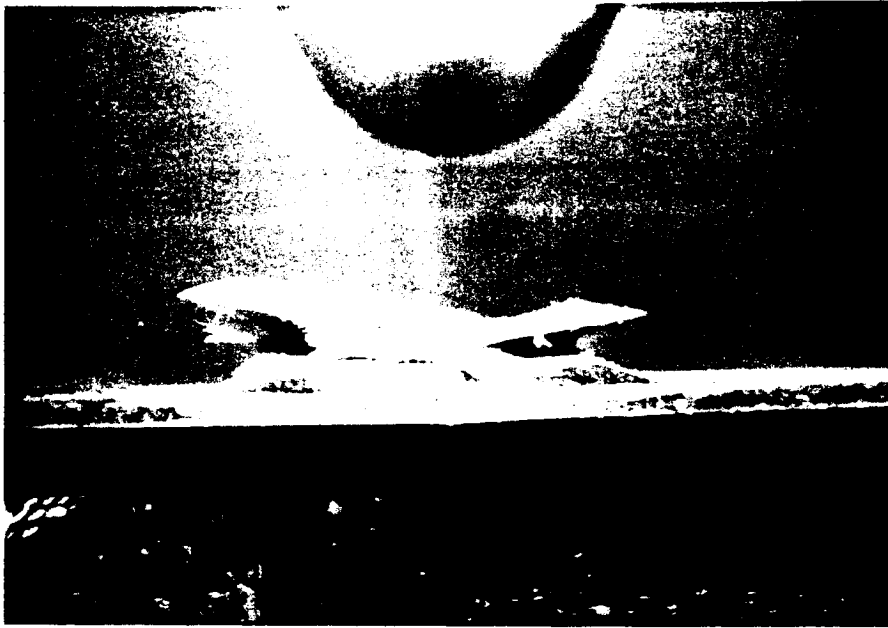


Figure 14. Pad damage Beam 1.

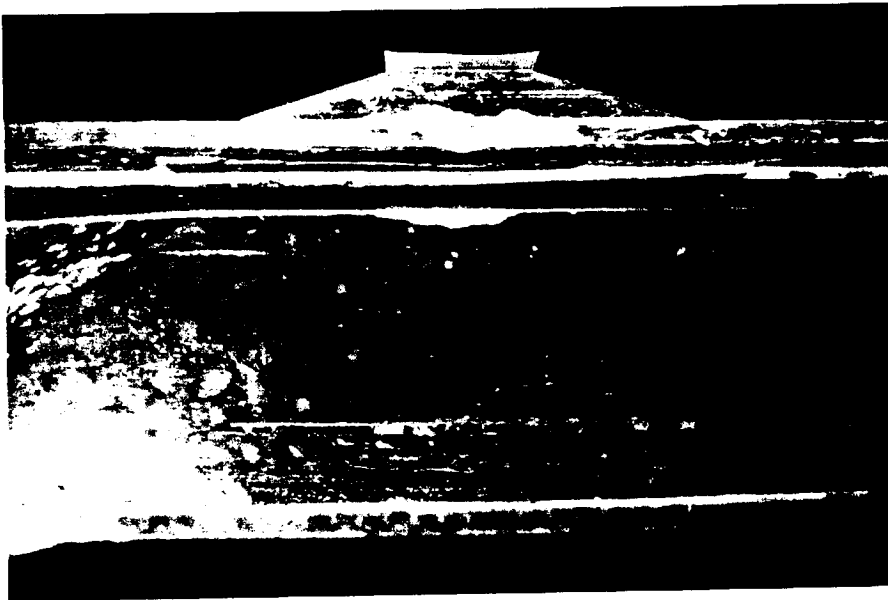


Figure 15. Compression damage zone, tension side, Beam 1.

Failure of Beam 1 resulted in massive damage in the shear web, separation of the outer-flange from the flanges of the C-channels and growth of the compression damage zone under the load pad (Chapter 4, Fig. 42). It was hypothesized that the initial compression damage was a nucleation site for crack growth in the adhesive joint between the outer flange and the flanges of the C-channel. Under cycling, cracks extend, releasing the tension flange from the C-channel flanges and the next stroke of the piston crushed the shear web.

Beam 2 was manufactured and tested to judge the validity of the hypothesis. The testing of Beam 2 was terminated before failure due to the growth of damage zones on the tension side flange immediately center of both support pads. Beam 2 was dissected and it was conclusively established that the aforementioned damage was failure of the tension flange adhesive joint. Visual inspection revealed a smooth fracture surface, indicative of an adhesive line failure as opposed to a rough fracture surface which would indicate matrix damage (Fig. 16). Therefore, the original hypothesis was incorrect and Beam 1 failed due to adhesive failure at the interface of the flanges.

Second Iteration

The adhesive failure of Beams 1 and 2 called for a re-design of the beam. The deflection equation for four-point bending, Equation 2.7, reveals that reducing the value I_{zz} of the beam by a factor of n allows for a reduction of the load by the same factor to achieve the same deflection. Also recall that $\epsilon = f(k, y)$, i.e., for a given curvature/deflection the strain is a linear function of y . I_{zz} was reduced by narrowing the flange width from 3 to 2 inches (now equal to the flange width of the C-channels) and incorporating two 0° ply drops in the gage section of the flange (Fig. 17). The ply drops reduced flange thickness to 0.13 inches from 0.17 inches. The resulting cross

sectional area in the gage section of the beam was reduced by approximately 0.5.

Ply terminations were molded in the flat plate mold (Appendix A). Uni-directional fabric was approximately 0.020 inches thick. Two sheets of 0.020 inch thick polycarbonate were temporarily bonded to the tempered glass of the mold (Fig. 18). The outer two layers of uni-directional fabric were cut to appropriate length, terminating at the respective layer of polycarbonate.

The addition of ply drops to the list of experimental parameters was desirable as they are used extensively in the fabrication of wind turbine blades. Ply drops are commonly employed in any composite structure where a decrease in laminate thickness is required. Additionally, it was hoped that the ply drops would facilitate flange failure in the gage section, away from the load pads.

During the testing of Beam 3, see Table 11 for test history, delaminations (Fig. 19) were severe at the ply drops on the tension side of the beam. There is an opening mode component to the delamination crack on the tension side of the beam, which favors delamination. Delaminations did occur on the compression flange of Beam 4, in the 10^6 cycle range. Delaminations were repaired when the size reached a subjective threshold as continued growth could have resulted in an undesirable failure mode. As mentioned in Chapter 2, Hysol EA9412, low viscosity epoxy was employed in delamination repair. Visual inspection of the repaired delaminations showed good wetting yet re-initiation and further delamination growth could not be suppressed. A single layer of chopped mat was applied on top of all ply drops in a vain attempt to inhibit delamination. Crack development in the adhesive joint of the tension flange, as reported in previous beams, appeared at approximately 400,000 cycles 20. Continued growth of this damage dictated a design change. Testing was stopped at 757,239 cycles, prior to failure.

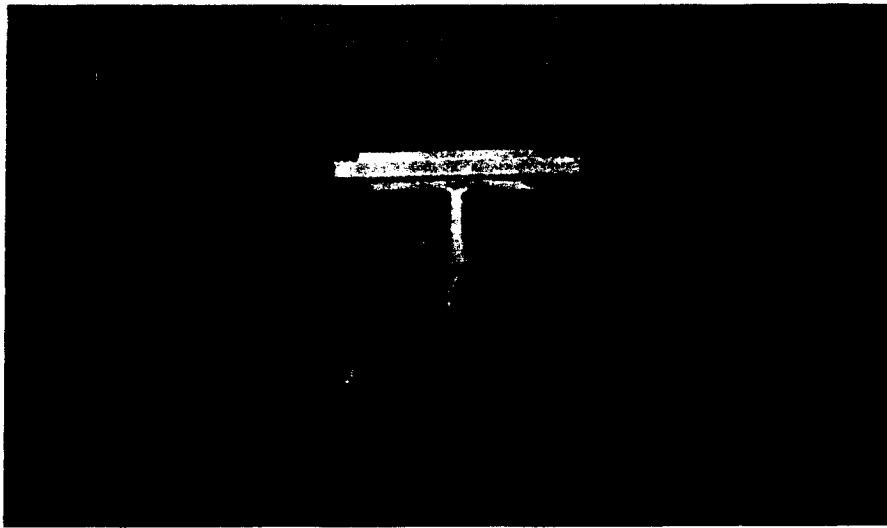


Figure 16. Shear failure of adhesive line, Beam 2.

Total Cycles	Cycles (Sequence)	Maximum Load (lbf)	Event
1			Strain Data
2-10,000	10,000	5,000	Increase Load
10,000-59,700	49,700	8,000	Ply Delamination
			Strain Data
59,700-757,239	697,539	8000	Test Terminated

Table 11. Test history Beam 3.

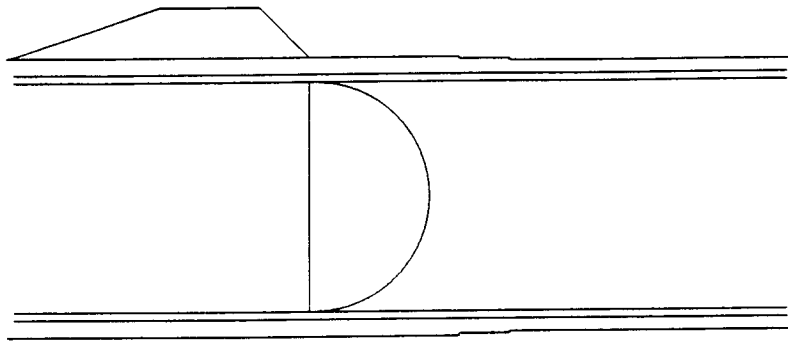


Figure 17. Ply drops, Configuration 3, xy plane.

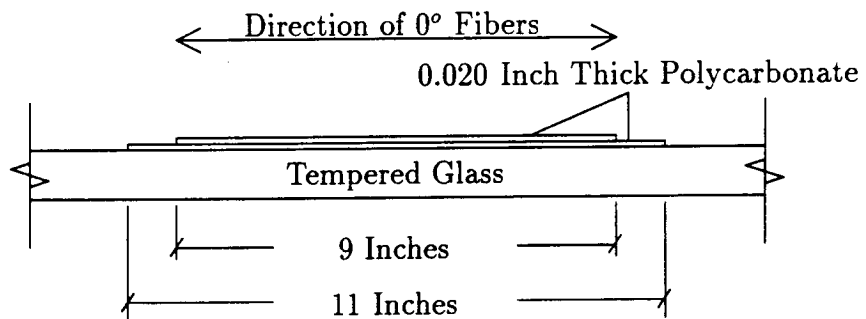


Figure 18. Front view of tempered glass from flat plate mold with polycarbonate sheets attached for ply terminations.

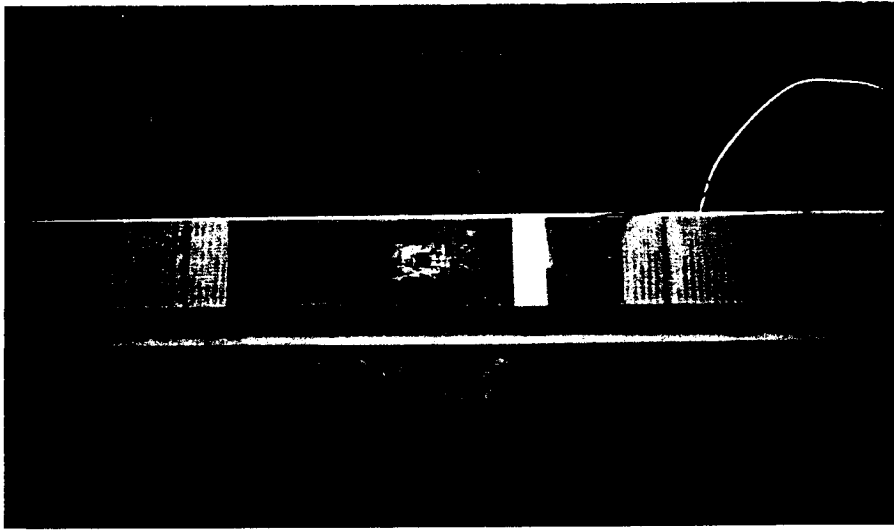


Figure 19. Delamination of ply drops, Beam 3.

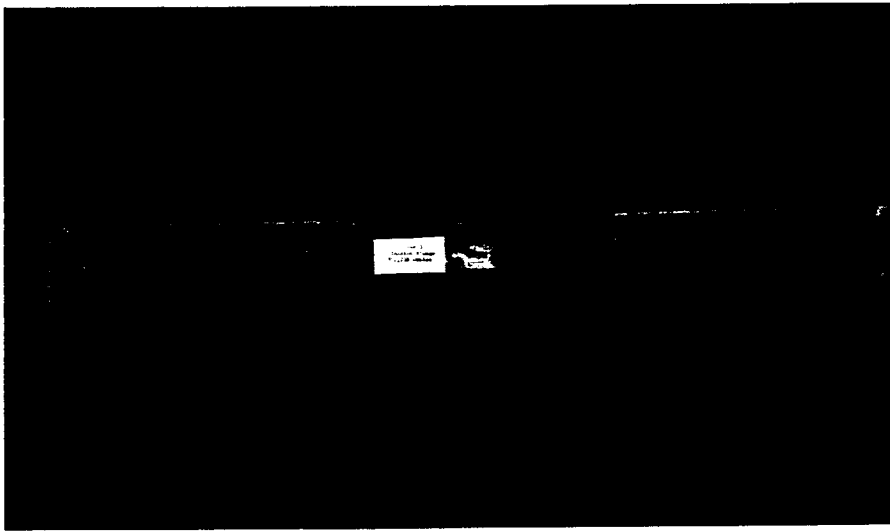


Figure 20. Shear damage in adhesive layer, tension flange, Beam 3.

Shear Failure at the Flange Adhesive Line

While Beam 3 was tested close to 10^6 cycles, it was apparent that conducting tests at higher strains and/or cycles would require further reduction of shear stress at the flange interface. A shear force diagram for four-point bending describes constant shear between the supports and the points of load introduction. The design of shear stiffener 1 created a complex geometry immediately above the tension flange and center of the outside support, with greatly reduced web thickness (Fig. 12). Constant thickness of the shear web/stiffener between the outside support and load pad would provide a constant cross section for distribution of the shear force.

Closed form approximate analysis [18] of shear stresses for open section members describes the stress distribution in terms of a single in-plane stress that is assumed constant through the thickness. The shear distribution for an I section predicts maximum flange shear stress at the intersection of the web and flange [18]. FEA of the interface between the outer flange and the C-channel flanges corroborates the closed form solution regarding the lateral location of maximum shear stress. Complete resolution of the FEA shear stresses depicts a complicated shear stress distribution which provided insight as to the cause of the shear failure and reinforced the selection of the proposed design solution, i.e., shear stiffener 2 (Fig. 12).

The shear stress concentrations that appear in Figs. 21-25 under the tension flanges, are most severe, by a factor of 3, for Configuration 2, having shear stiffener 1. Similar results were obtained for Configuration 1, which also employed stiffener 1. Fig. 21 shows the only shear stress concentration on the tension flange to be immediately in front of the support pad, $3 \leq x \leq 5$, corresponding to where the stiffener loses contact with the inner surface of the C-channel flange. The shear stress distribution for Configuration 3 shows two peaks, the larger occurring at the initiation of taper in the shear stiffener, $x = 7$ inches, again where contact is lost

between the inner-surface of the C-channel flange and the surface of the stiffener. The smaller stress spike on this surface is located at the point of outside support, $x = 3$ inches. Stress spikes occur on all graphs at sites of thickness change of the shear web/stiffener, tension and compression flanges. The redesign from Configuration 2 to Configuration 3 reduced the maximum XY shear stress from about 1400 psi to about 600 psi at 4000 lbs load. This effectively solved the adhesive failure problem.

Figs. 23-24 depict the XZ component of the shear stress at the flange interface for Configurations 2 and 3. The magnitude of shear stress XZ is not appreciably affected by the different shear stiffeners, although the distribution is affected. Furthermore, the magnitude of this component of shear stress is significant.

For completeness, Fig. 25 shows that the YZ component of the shear stress, Configuration 3, is negligible. This is consistent with the xy symmetry boundary conditions imposed on the FEA. Minimal YZ shear was found for all configurations.

The FEA predicted a significant stress concentration at the exact site, the adhesive layer under the outside support on the tension flange, of crack initiation in Configurations 1-2, employing shear stiffener 1. The outer flanges in the FEA mesh were a single element thick, with orthotropic material properties. Outer flange elements shared common nodes with the orthotropic elements defining the flanges of the C-channel, with distinct orthotropic material properties. The adhesive was not modeled. Investigation of the possible influences of material discontinuity at the shared nodes was warranted. Additionally, curiosity is piqued when noting the change in sign of shear stress XY acting on the compression flange at $x = 5$ inches in the z direction (Figs. 21,22). The shift in sign of the XY shear stress is similar to that predicted by closed form solution [18], for a Z-section. To determine the role of material discontinuity, FEA was completed for Configuration 2 with the isotropic material properties of aluminum substituted throughout. Shear stress XY results

(Fig. 26) demonstrate that material discontinuity does not affect the FEA shear stress solution on this plane. (All FEA concerning the shear failure of the flange adhesive joint were run with an equivalent total load of 4,000 lbf.)

Beam 4

Beam 4 included shear stiffener 2 and ply-drops, it was the final design of this project. The change in shear stiffener shape completely eliminated any signs of shear failure in the flange adhesive joint, validating the FEA. Delamination of the ply drops was a chronic problem with this beam, one which was never adequately resolved. Load pad failure at 1.3 million cycles was unexpected and catastrophic for all pads. Steel layers 0.125 inch thick were connected to a new set of composite pads using epoxy adhesive and machine screws; screw holes were taped. The steel pads did spall, but no further problems occurred with the load pads for the duration of testing. Beam 4 was tested to failure in fatigue (Tables 12-13).

Beam 5 - Static Test

Beam 5 was tested to failure in a static ramp loading test, although three attempts were required to achieve failure. Piston displacement approached 0.5 inches at failure. This large deflection presented unexpected difficulties. At 20,000 lbf the first attempt was terminated by failure of a fixture end constraint (Appendix B). Damage to the test specimen was limited to a 4 inch delamination, top surface of the compression flange, extending from the end of the beam that contacted the failed constraint. The delamination was repaired as previously described and the end constraints were removed from the test fixture. The second attempt had the beam slip off the load rollers, which initiated an axially directed translation. It is believed that this translation caused the end constraint failure in the initial test. The explanation

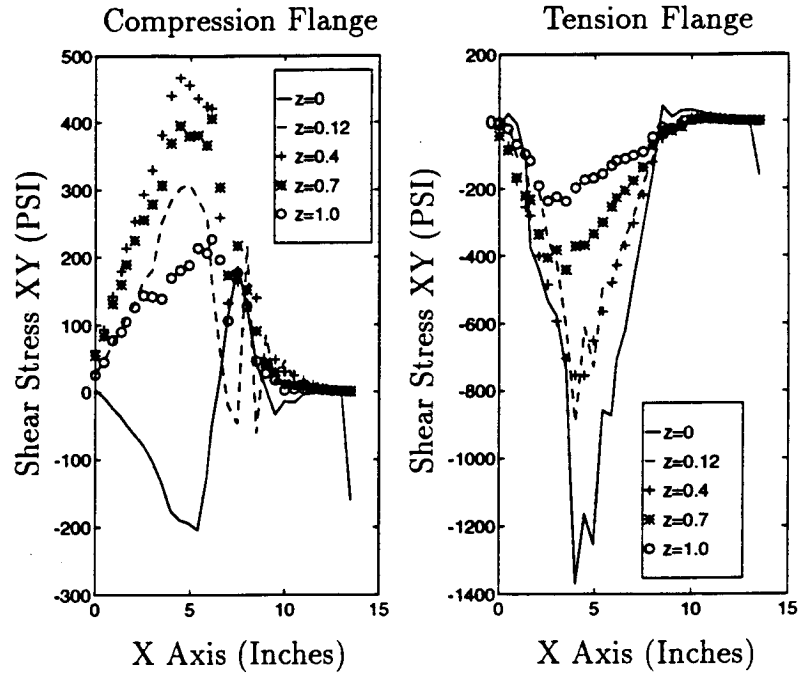


Figure 21. Shear stress XY at the adhesive interface of flanges, Configuration 2.

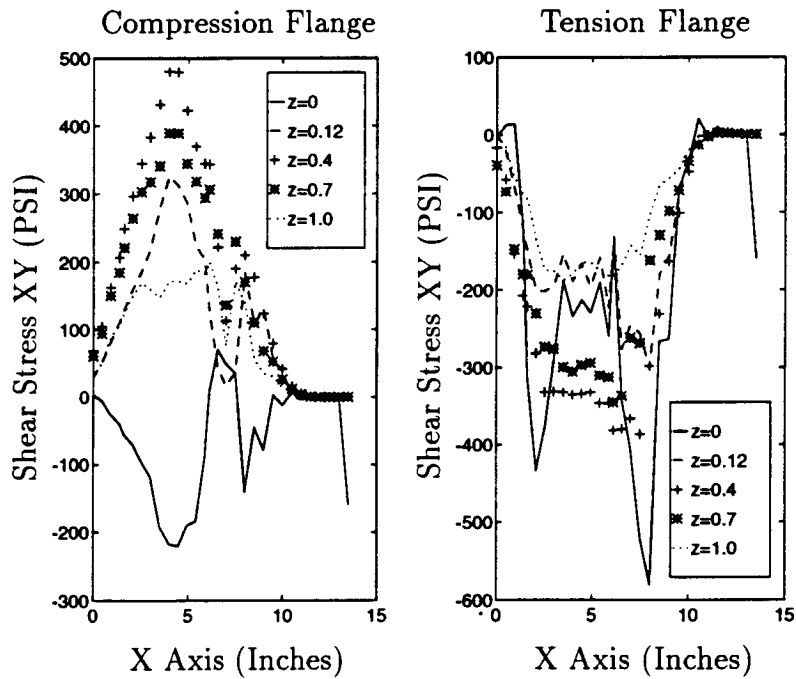


Figure 22. Shear stress XY at the adhesive interface of flanges, Configuration 3.

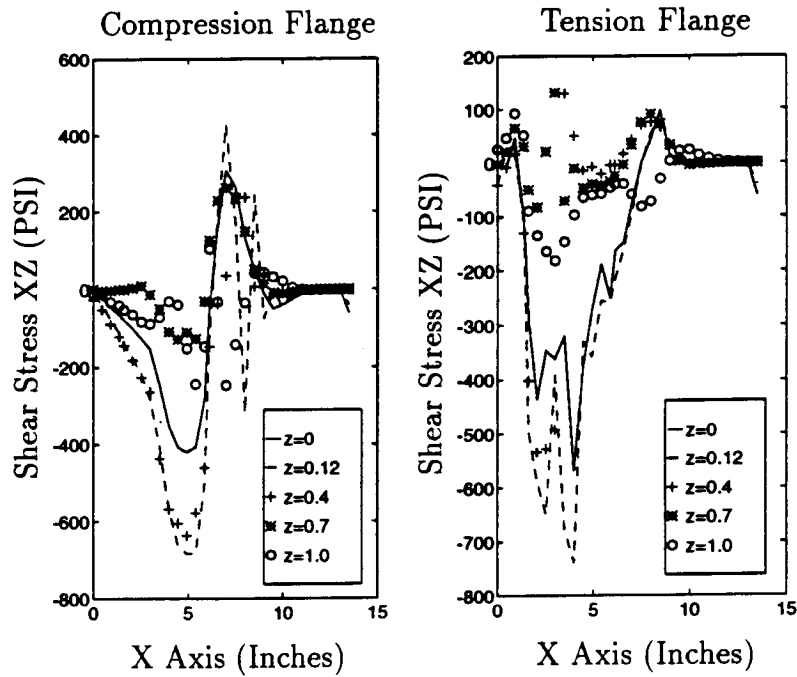


Figure 23. Shear stress XZ at the adhesive interface of flanges, Configuration 2.

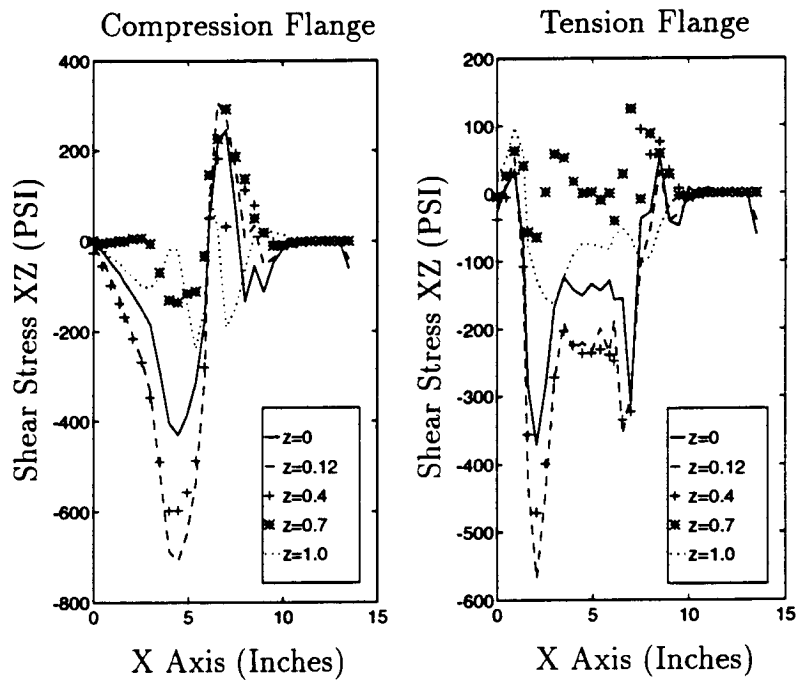


Figure 24. Shear stress XZ at the adhesive interface of flanges, Configuration 3.

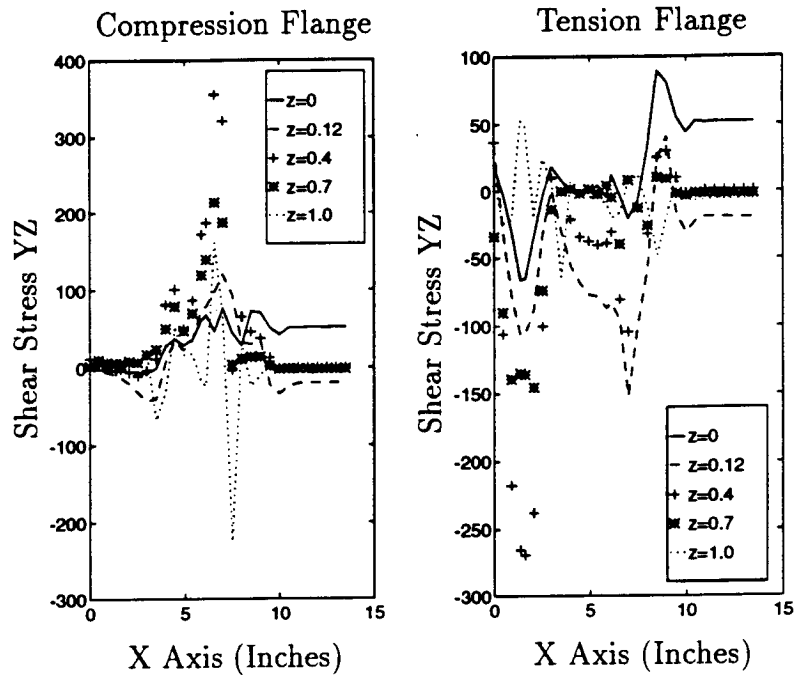


Figure 25. Shear stress YZ at adhesive interface of flanges, Configuration 3.

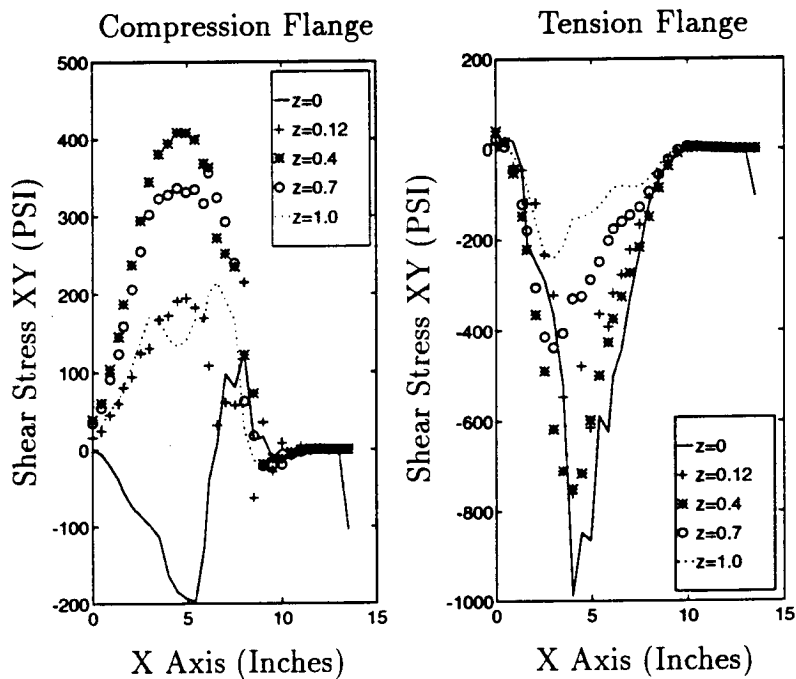


Figure 26. FEA shear stress XY at flange interface, Configuration 2, with isotropic material properties.

Total Cycles	Cycles (Sequence)	Maximum Load (lbf)	Event
1			Data
			Apply Mat
			Data
2-10,000	10,000	5,000	Increase Load
10,000-500,000	490,000	8,000	Repaired Delams
			Data
500,000-779,102	279,102	8,000	Data
779,102-1.2e6	392,227	8,000	Repaired Delams
			Data
			Increased Load
1.2e6-1.3e6	171,715	9,000	All Pads Failed
			Repaired Beam
			Increased Load
1.3e6-1.6e6	300,000	10,000	Data
			Repaired Delams
			Data
1.6e6-1.76e6	160,000	10,000	Repaired Delams
1.76e6-1.97e6	200,000	10,000	Repaired Delams
			Data
			Increased Load
1.97e6-2.24e6	269,977	11,000	Data
2.24e6-2.26e6	16,354	11,000	Beam Failed

Table 12. Test history Beam 4.

Maximum Load (lbf)	Micro-Strain (average of tension and compression)	Cycles at Load	Total Cycles
5,000	4040	10,000	10,000
8,000	6360	1.16e6	1.17e6
9,000	7180	171,715	1.34e6
10,000	8270	631,360	1.97e6
11,000	9220	285,735	2.26e6

Table 13. Load, micro-strain and cycles summary, Beam 4. Micro-strain values are the average magnitudes of tension and compression strain measured at the initiation of each sequence.

for this occurrence of slip is found in the asymmetric design of the load pads (Fig. 12) coupled with large deflections and corresponding shortening of the compression flange. All pads were removed and replaced with rectangular shaped pads measuring 2 by 3 by 0.51 inches. The third loading did result in failure of the beam, described in Chapter 4.

CHAPTER 4

RESULTS AND DISCUSSION

Overview

As mentioned in Chapter 2, initial design considerations did not include the effects of shear deflections in the response of the beam to loading. For this chapter the shear and bending deflection equations from beam theory were solved for a composite I-beam. This allows for a thorough comparison of beam theory, FEA and experimental results. Damage development in the beams is described in chronological order: ply-drop delaminations, off-axis ply cracking, failure of axially oriented fibers and final beam failure. As a result of damage development a corresponding change in beam stiffness was observed. Two distinct mechanisms were identified as effecting beam stiffness: adhesive failure of the flange joint (see Chapter 3), resulting in a premature stiffness change that was both experimentally and theoretically bothersome until identified, and stiffness change due to damage in the composite material. Stiffness change due to damage development progressed in a manner similar to that observed by other researchers. Strain gage failure at approximately the 13,000 micro-strain level was documented during the static loading test of Beam 5. Fatigue and static failure modes are described and contrasted. Finally, a comparison of fatigue results for material tested in coupon and beam geometry is presented.

Deflection Curve Equation

In order to include deflections predicted by classic beam theory in the following discussion for Beams 4 and 5, the differential equations of the deflection curve for a

beam, expressed in terms of shear force and bending moment [22] were integrated. The flexural rigidity term, EI , was derived following Equation 2.6. Additionally, the differential equation describing the displacement effects of shear deformation [23], modified for a composite beam is expressed as,

$$\frac{dV}{dx} = \frac{\alpha_s V}{\sum_{i=1}^n G_i A_i}. \quad (4.1)$$

Equation 4.1 was integrated and included in the deflection solution. The derivation of the composite shear rigidity ($G_i A_i$) in Equation 4.1 was premised on the same principals as that of the composite flexural rigidity.

On the interval $0 \leq x \leq a$ the total displacement solution is given by

$$\nu_1(x) = \frac{Px}{6} \left[\frac{3a(L-2a)}{(EI)_2} + \frac{3a^2 - x^2}{(EI)_1} \right] + \frac{\alpha Px}{(GA)_1} \quad (4.2)$$

and for the interval $a \leq x \leq \frac{L}{2}$ the displacement is given by

$$\nu_2(x) = \frac{Pa}{2(EI)_2}(Lx - x^2) + \frac{Pa^3}{6} \left[\frac{2}{(EI)_1} - \frac{3}{(EI)_x} \right] + \frac{\alpha Pa}{(GA)_1}. \quad (4.3)$$

Theoretical, FEA and Experimental Comparisons

A comparison of experimental, FEA and beam theory micro-strain (at the outside surface, center of the flanges) vs load slopes for Beam 2 is presented in Table 14, taken from Fig. 35. Experimental results from Beam 2 are those recorded during the first cycle of testing. The close correlation of beam theory with both FEA and experimental results (3% maximum variation) is surprising in light of the length-to-depth (l/d) ratio of the beam. Recall that shear deformation effects were not incorporated in the initial beam theory predictions. These results indicate that shear stiffener 1 was effective in eliminating shear deflections.

That shear stiffener 2 effectively suppressed shear deformation in Beams 4 and 5 is supported by the last term in Equation 4.2, the shear deflection component. The shear component of deflection at 8,000 lbf total load is approximately 5% of the total deflection at the loadpads. Also, beam theory and experimental micro-strain results for Beams 4 and 5 vary by only 8%, Table 16. If shear deformation was of significant magnitude these micro-strain values would not be in such close agreement. It should be noted that correlation of theoretical micro-strain and FEA results for Beams 4 and 5 is not as close as for Beam 2, yet the agreement is still generally good.

It is interesting to note that both beam theory and FEA predict a similar deflection curve that varies from the experimental, Table 15. Both FEA and beam theory predictions underestimate the displacements at the loadpads and overestimate the deflection at the center of the beam. Equation 4.3 predicts a center point displacement that is 23% greater than the average value recorded in the laboratory.

In contrast to the close correlation of experimental and predicted results for Beams 2,4 and 5 are the micro-strain results for Beams 1 and 3, Tables 17-18, taken from Figs. 35-36. First cycle comparison of Beam 3 micro-strain results with FEA results, Table 18, shows a 15% discrepancy in slope values. Beam 1 at 100,000 cycles (initial micro-strain data was not gathered for Beam 1) shows a 13% variation between experimental and FEA tensile micro-strain results, Table 17. The compressive micro-strain slope value for Beam 1 at 100,000 cycles is at an acceptable 8% variation from experimental. The most plausible explanation for these discrepancies is variation in the manufacturing process. The change in experimental boundary conditions at 200,000 cycles for Beam 1 (when the outside rollers were installed in the test fixture) would account for a less stiff beam, more closely matching the boundary conditions of the FEA and possibly accounting for part of the 9% shift in the tensile micro-strain curve for this beam. However, this reasoning is inconsistent with the compressive

	Slope of Strain vs. Load Curve ($\mu\epsilon$ /Thousand Pounds)		Ratio of (Slope/Experimental Slope)	
	Tension	Compression	Tension	Compression
FEA	381	384	1.01	1
Classic	387	387	1.03	1
Experimental	376	384	1	1

Table 14. Comparison of FEA, beam theory and experimental strain vs load slopes, Beam 2.

	Avg. Experimental Slope Values	Predicted Slope	
	(inch/ 10^3 lbf)	Theoretical	FEA
Displacement	(inch/ 10^3 lbf)	(inch/ 10^3 lbf)	
Load	.0228	.0182	.0183
Center	.0359	.0442	.0396
Micro-Strain	($\mu\epsilon/10^3$) lbf	($\mu\epsilon/10^3$ lbf)	
Tension	825	888	880
Compression	828	888	881

Table 15. Comparison of FEA, beam theory and average 1st cycle experimental displacement and micro-strain vs load slopes, Beams 4 & 5.

	Ratio of Slopes	
	(Theoretical/ Avg. Exp)	(FEA/ Avg. Exp)
Displacement		
Load Point	0.8	0.8
Center	1.23	1.10
Micro-Strain		
Tension	1.08	1.07
Compression	1.07	1.06

Table 16. Ratios of predicted displacement and micro-strain slopes over average experimental slopes for Beams 4 and 5. The experimental slopes listed are those derived from the 1st cycle of testing.

	Slopes of Load vs Strain Curve $\mu\epsilon$ /Thousand Pounds		Ratio of Slopes
	FEA	Beam 1	FEA/Experimental
Tension Cycles			
1	381		
100,000		336	1.13
200,000		366	1.04
Compression Cycles			
1	384		
100,000		363	1.06
200,000		360	1.07

Table 17. Comparison of FEA and experimental strain vs load slopes, Beam 1.

	Slopes of Load vs Strain Curve $\mu\epsilon$ /Thousand Pounds		Ratio of Slopes
	FEA	Beam 2	FEA/Experimental
Tension Cycles			
1	880	760	1.15
59,700		853	1.03
Compression Cycles			
1	881	750	1.15
59,700		760	1.17

Table 18. Comparison of FEA and experimental strain vs load slopes, Beam 3.

Slope of Displacement vs Load Curves (Inches/Thousand Pounds)								
	FEA		Theoretical		Beam 4		Beam 5	
	Load	Center	Load	Center	Piston	Center	Piston	Center
Cycles								
1	.0183	.0396	.0182	.0442	.0238	.0356	.0218	.0362
2							.0235	.0372
3							.0219	.0356
1.17e6					.0242	.0371		
1.97e6					.0260	.0397		
2.24e6					.0308	.0465		

Table 19. Comparison of FEA, theoretical and experimental displacement vs load slopes, Beams 4 & 5.

Slope of Strain vs Load Curves ($\mu\epsilon$ / Thousand Pounds)				
	FEA	Theoretical	Beam 4	Beam5
Tension Cycles				
1	880	888	823	826
2				836
3				823
1.1e6			823	
1.9e6			912	
2.24e6			913	
Compression Cycles				
1	881	888	803	853
2				889
3				870
1.1e6			816	
1.1e6			854	
1.1e6			827	

Table 20. Comparison of FEA, theoretical and experimental micro-strain vs load slopes, Beams 4 & 5.

micro-strain data for Beam 1, which did not appreciably change after introduction of the outside roller supports, and the 15% variation in 1st cycle results for Beam 3, which was tested with all roller supports throughout its testing regime. The consistency of 1st cycle experimental results for Beams 4 and 5, Tables 19-20 taken from Figs. 37-40, does demonstrate repeatability in the manufacturing process, which is vital for both experimental and composite production purposes. The observed variation between experimental and FEA micro-strain results may be explained by initial inconsistencies in the beam fabrication process.

Damage Development

Delaminations initiating at the ply-drops, on the tension flange of Beams 3-5 were the first signs of damage development in these beams. Ply-drop delamination was observed in Beam 3 after 50,000 cycles (6000 $\mu\epsilon$), and after 10,000 cycles (6000 $\mu\epsilon$), Beam 4. Tension side ply-drop delaminations occurred on Beam 5 (static test) at 20,000 lbf (approximately 15,000 $\mu\epsilon$). Minor delaminations did occur on the compression flange ply-drops of Beams 3, but did not grow to significant size. At 1.3 million cycles on Beam 4, compression flange delaminations were not of sufficient size to warrant repair. However, at 1.7 million cycles (460,000 cycles at 10,000 $\mu\epsilon$, Table 12) the compression delaminations were of sufficient size that repair was completed, as further growth would have jeopardized the structure. The compression ply-drops of Beam 5 showed no signs of delamination during the three static tests on this beam.

Just as in testing composite materials in coupon geometry which contain off-axis plies, one of the first signs of damage development in all beams, aside from ply-drop delaminations and flange adhesive failure (previously discussed in Chapter 3), was cracking of the ± 45 layers of the C-channel flanges, or first ply failure. First ply failure is a tension related phenomena that is well explained by viewing the stress

state in an off-axis ply from the perspective of its local ply coordinates, i.e., a stress transformation from the laminate coordinates to that of ply coordinates (Fig. 6). Consider a laminate with off-axis plies subjected to pure bending. In the off-axis ply orientation there exist a tensile stress normal to the fibers and an in-plane shear stress, both of which act to cause transverse debonding of the fiber from the matrix and cracking of the matrix [15]. Extensive damage in the ± 45 layers of both flanges was observed at 200,000 cycles in Beam 3 and 350,000 cycles in Beam 4. All beams exhibited an accelerated accumulation of damage in the ± 45 layers of the tension flange relative to the compression flange (Figs. 27-30). The difference in rate of crack development in the tension and compression flanges is directly attributable to the transverse tensile stress component in the $\pm 45^\circ$ plies of the tension flange, as opposed to the transverse compressive stress stress in the off-axis plies of the compression flange.

After approximately 200,000 cycles at approximately $6000 \mu\epsilon$, longitudinal cracks were observed in the top surface of the compression flange of Beam 3, approximately mid-width in the area of the ply-drops. These cracks did propagate towards the center of the beam with cycling; the longest crack achieved a length of 2 inches at the termination of testing, 750,000 cycles. Similar cracks developed in the compression flange of Beam 4 (Fig. 32), but were not observed until approximately 900,000 cycles. After failure of Beam 4 one of the longitudinal cracks on the compression flange extended from the front of the loadpad to the center of the beam, approximately 6.5 inches. Inspection of Beams 4 and 5 after failure revealed longitudinal cracks in the tension flanges of both beams also (Fig. 31). The tension flange of Beam 5 showed a number of these cracks extending from the outside support pads towards the center of the beam, covering the width of the beam. The compression flange failure of Beam 5 (Fig. 44) eliminates the possibility for observing longitudinal

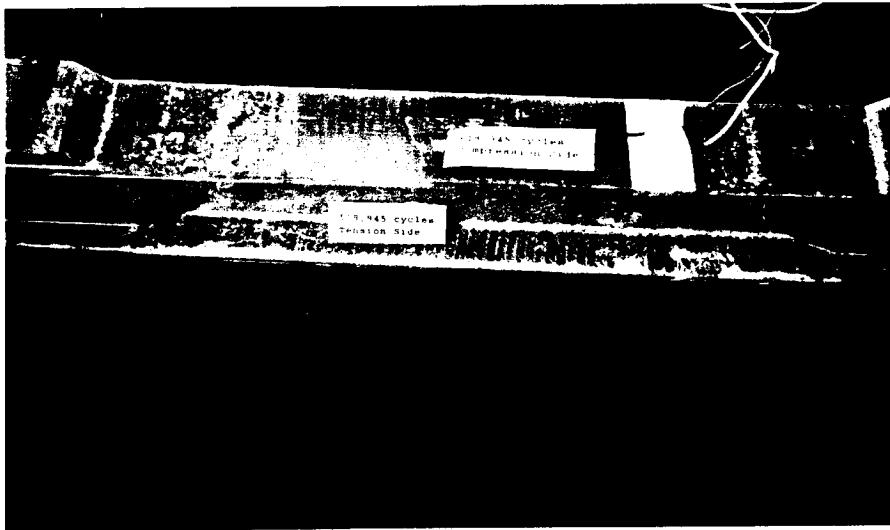


Figure 27. Accumulated damage on inner surface of tension flange, off axis plies, 518,945 cycles, Beam 4.

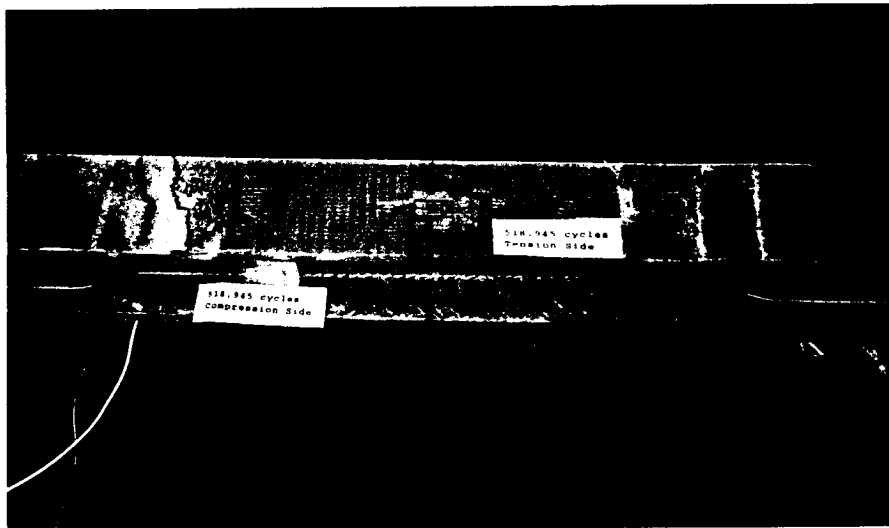


Figure 28. Accumulated damage on inner surface of compression flange, off axis plies, 518,945 cycles, Beam 4.

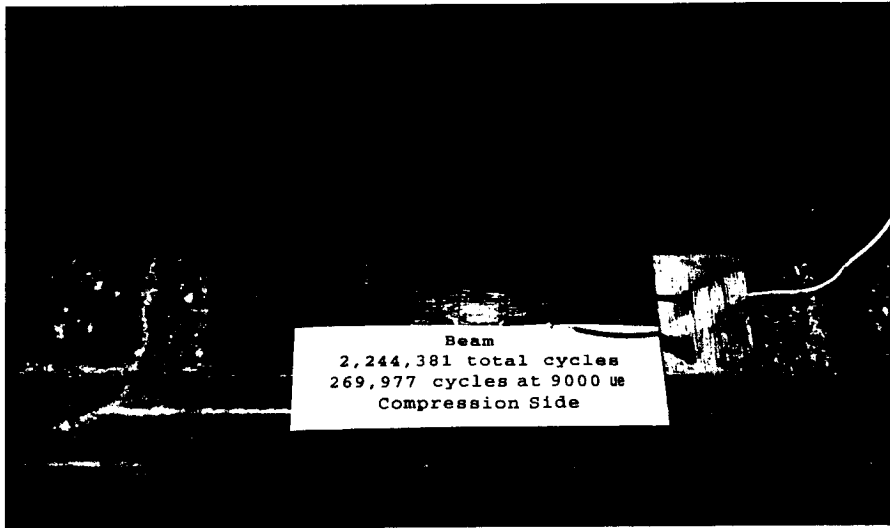


Figure 29. Accumulated damage on inner surface of tension flange, off axis plies, 2.24 million cycles, Beam 4.

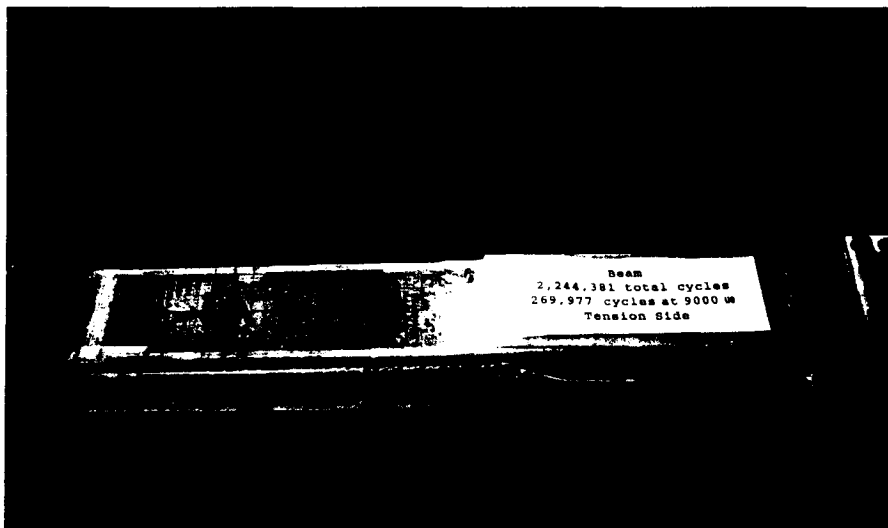


Figure 30. Accumulated damage on inner surface of compression flange, off axis plies, 2.24 million cycles, Beam 4.

cracks in this flange after failure.

The effects of transverse strain coupled with either the constraint of the web or perhaps more likely the constraint of the off-axis plies in the flange of the beam is the most probable explanation for these cracks. Transverse strain in a beam is expressed as [24],

$$\epsilon_z = \nu_{xy}ky. \quad (4.4)$$

The compression flange experiences positive transverse strain and the tension flange negative transverse strain. If unconstrained, as with an isotropic material, this strain is simply a Poissonic material response with no resultant stress. However, in a laminate containing off-axis plies, the fibers of the off-axes plies resist this expansion/contraction resulting in compressive and tensile stress in the 0° plies for respective tensile and compressive loadings. From a laminate perspective the net stress in the y direction must still be zero to match the boundary conditions. Similar to first ply-cracking, the effect of these strains would be for longitudinal cracking in the compression flange to precede similar cracking in the tension flange, as did occur.

At approximately 900,000 cycles broken 0° fibers (longitudinal fiber failure) was observed on the edge of the tension flange in the area of the ply-drops, Beam 4 (Fig. 31). The initial failure of the 0° fibers was most likely a result of stress concentrations and/or possibly abrasion at the sites of the ply-drops. At 2 million cycles separation of the broken 0° fibers from the flange had progressed to the center of the beam. Upon failure of the beam the strands had separated from the flange the distance of the gage section.

At 2.2 million cycles damage in the web of Beam 4, at the tip of the shear stiffener (Fig. 33) was observed in the typical form of opaque discoloration of the the matrix. As will be discussed in more detail in the Failure Modes section, this is believed to be the initiation of beam failure.

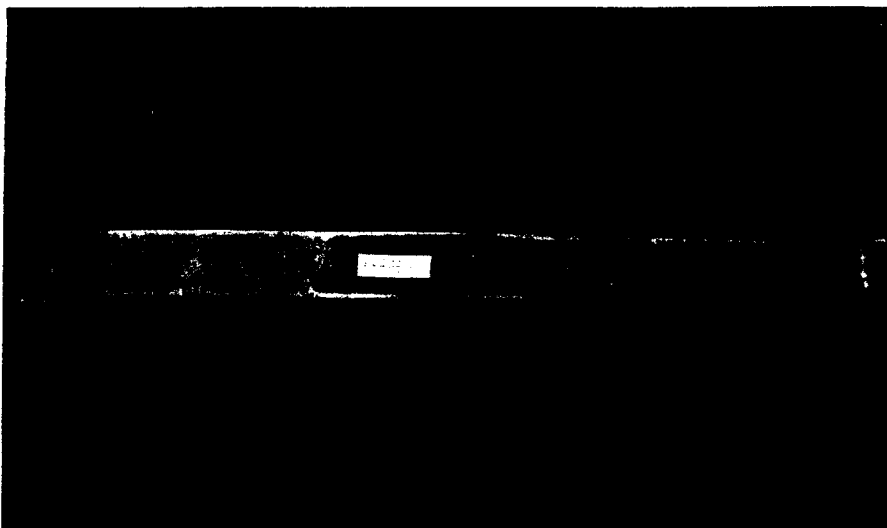


Figure 31. Outer surface of tension flange, 2.26 million cycles, Beam 4.

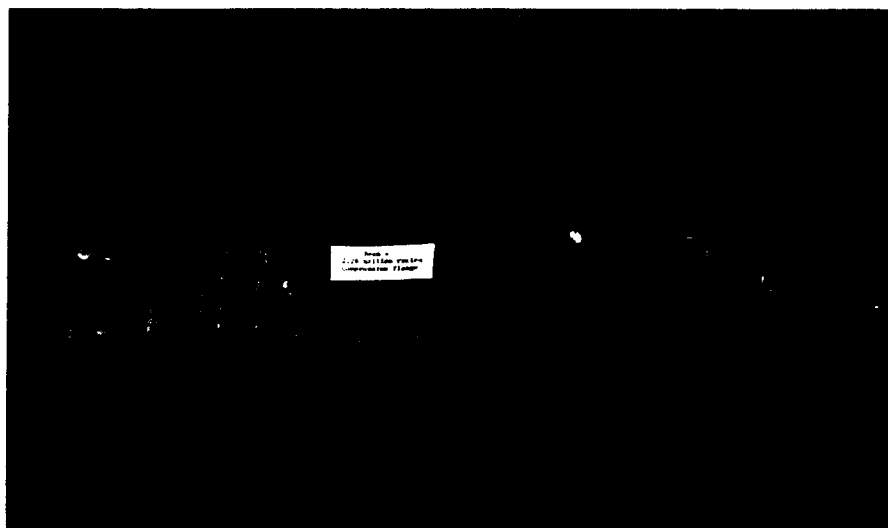


Figure 32. Outer surface of compression flange, 2.26 million cycles, Beam 4.



Figure 33. Damage in shear web of Beam 4, immediately in front of the shear web stiffener, at 2.2 million cycles.

Change in Stiffness

Beam 4 was tested at sufficient strain/stress and cycle levels to produce definite shifts in all data curves (Figs. 37-38 and Tables 19-20). Comparison of micro-strain vs load data for all beams shows a significant shift in the slopes of Beams 1-3 at much lower cycles relative to Beam 4. Fig. 34 shows dramatic contrast in behavior between Beams 3 and 4. This variation is directly attributable to the change in shear stiffener and the suppression of shear failure at the adhesive joint between C-channel flanges and the outer flanges (see Chapter 3 for details). Crack growth in the adhesive flange joints of Beams 1-3 was softening the beam, increasing the displacement and strain under load.

Flange materials were largely comprised of unidirectional fiber, Table 4, and previous research [25] indicates that decay in modulus of 0° dominated laminates is noticeable and precipitous only at the end of the lifetime of the laminate. This finding is corroborated by the results of Beam 4 (Figs. 34,37,38).

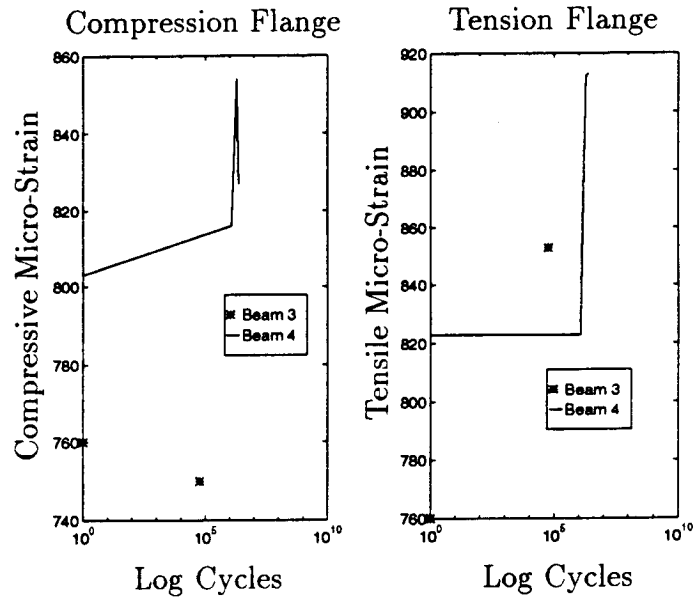


Figure 34. Change in micro-strain vs cycles, Beams 3 & 4. The sharp increase in the tension micro-strain values for Beam 3 is a reflection of the growth of adhesive failure in the flange interface due to shear.

At approximately 2 million cycles, immediately before failure, Beam 4 shows lower average stiffness than at lower cycles due to damage. However, the shape of the load-deflection and microstrain curves now shows a stiffening tendency with increasing load (Figs. 37,38). Coupon testing of graphite/epoxy based composites has demonstrated a nonlinear stiffening response in laminates dominated with unidirectional fibers and those of $[\pm\theta]$ layup with $\theta \leq 15^\circ$ [26]. However, coupon testing of glass/polyester laminates with off axis plies reveals a nonlinear softening response, attributed to damage in the off axis plies [27]. The stiffening behavior of Beam 4 is not a material response, it is a response to large deformations. Note that at 6000 pounds (Fig. 37) the display placement increases by almost 10% between 1.17 million and 1.97 million cycles and by approximately 20% between 1.97 and 2.24 million cycles. With increasing deflections a decreasing component of the applied load acts in bending, stiffening the response of the beam. This response is typical of nonlinear large deflection response in structures [28].

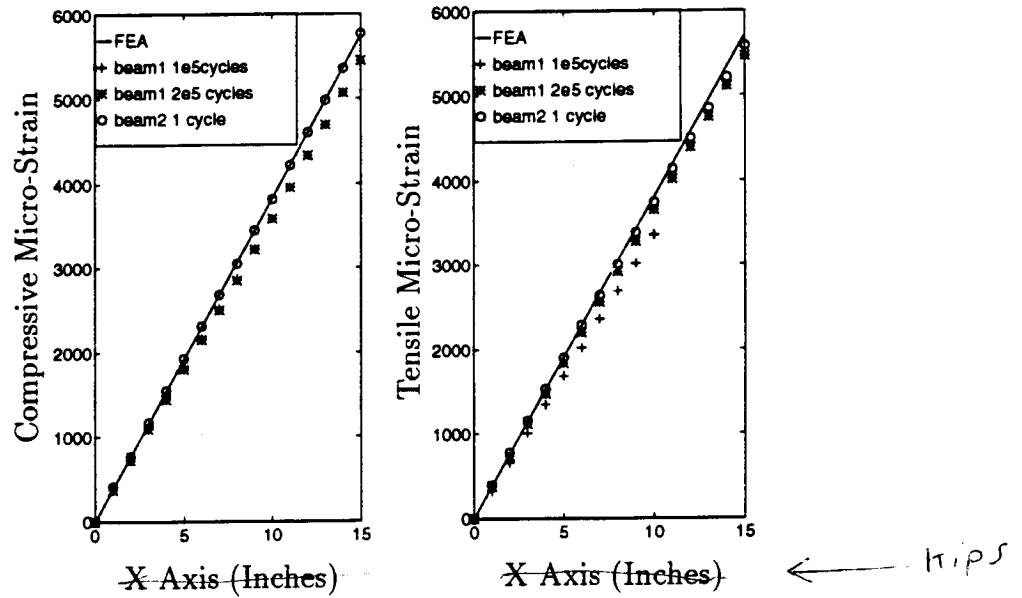


Figure 35. FEA and experimental strain vs load data, Beams 1 & 2.

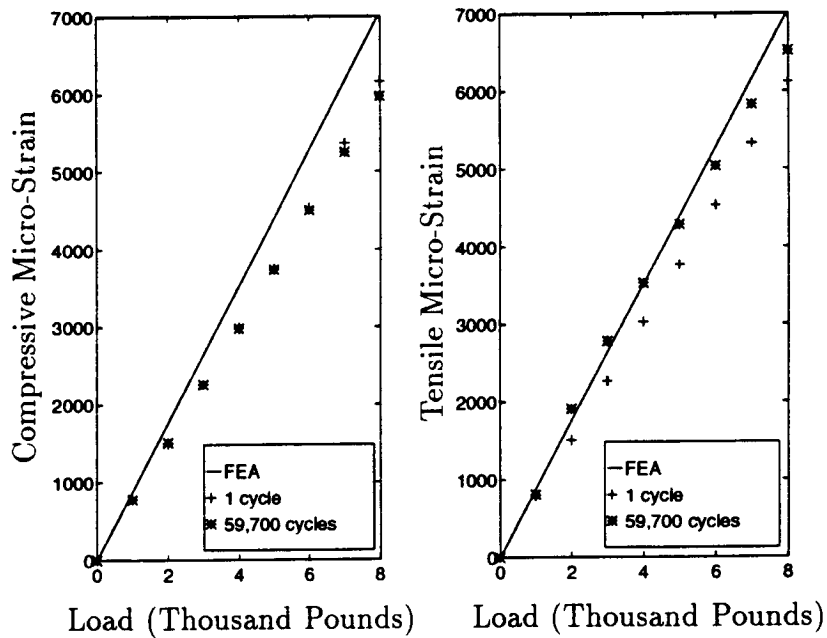


Figure 36. FEA and experimental strain vs load data, Beam 3.

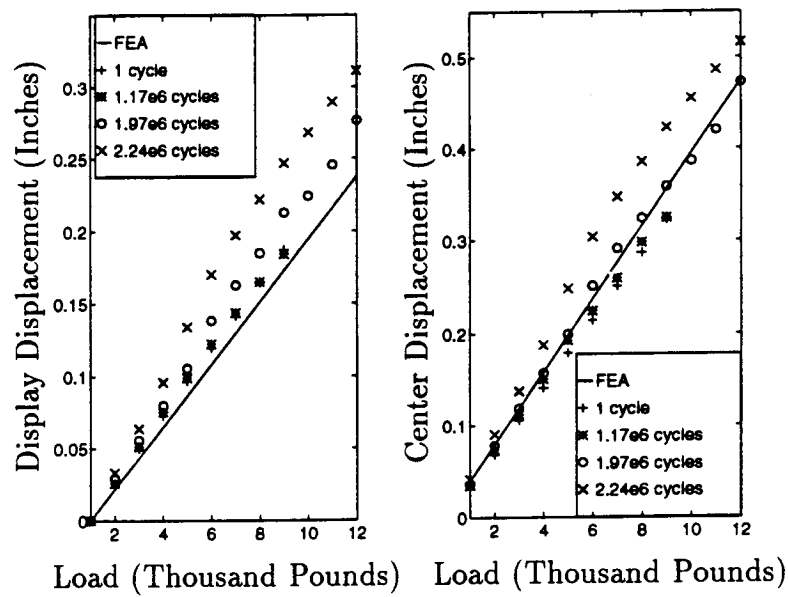


Figure 37. Piston and center point displacement vs load, Beam 4.

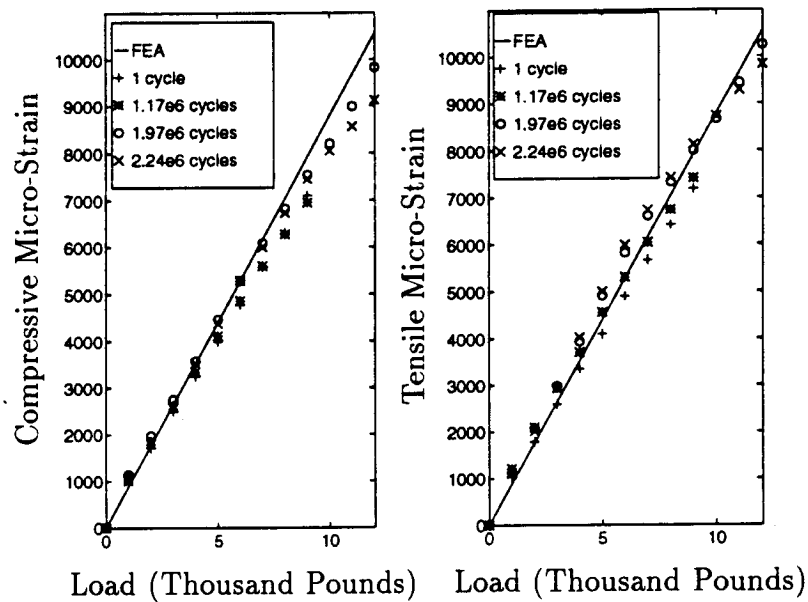


Figure 38. FEA and experimental micro-strain vs loads, Beam 4.

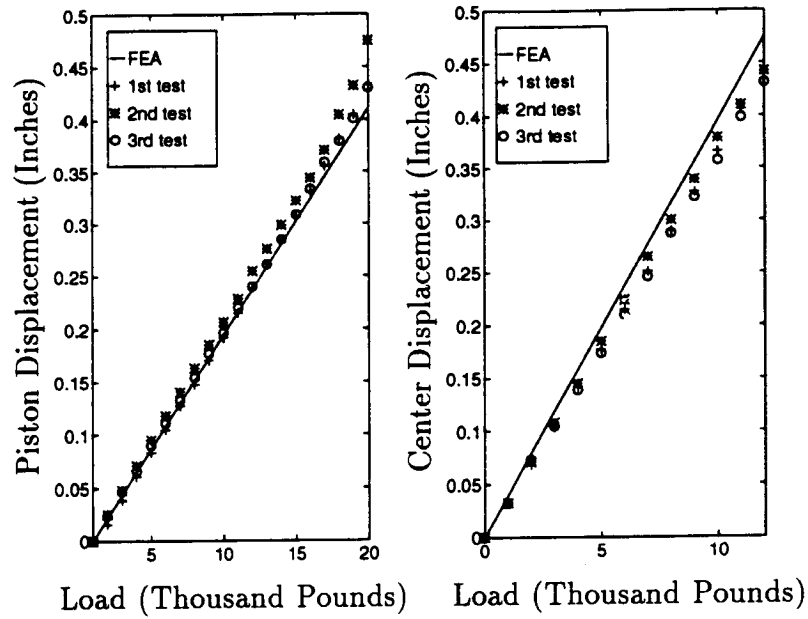


Figure 39. FEA and experimental displacement vs load results, Beam 5.

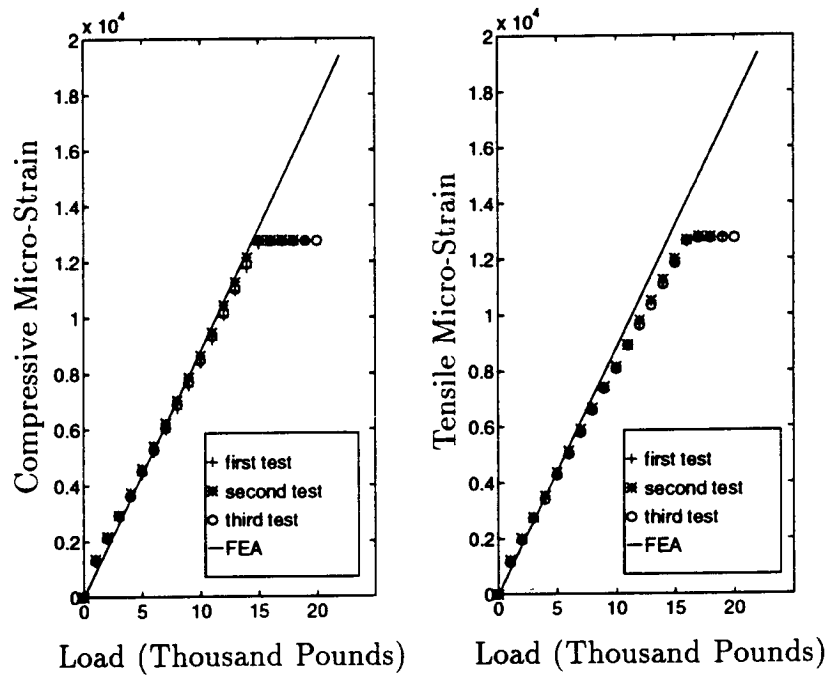


Figure 40. FEA and experimental strain vs load results, Beam 5.

Strain Gage Failure

The knee in the micro-strain graphs for Beam 5 (Fig. 40) is a result of strain gage element rupture and subsequent saturation of the electronics. This was verified by affixing the same type of strain gage to a composite coupon, made of gage section flange 2 material, and loading the coupon in tension in a test fixture. The output of the strain conditioning cards was recorded from the output display and via a digital volt meter (DVM) (Fig. 41). At approximately 12,000 $\mu\epsilon$ the milli-volt reading jumped to 12 volts. Upon unloading and reloading the coupon a similar linear response occurred up to 3000 lbf at which point the DVM output jumped to +12 volts and the display output registered 1200 $\mu\epsilon$. Strain gage elements were rupturing at 1200 $\mu\epsilon$ on the initial pull. The open leg of the wheatstone bridge, which was configured as a quarter bridge, resulted in a V_{out} of the same order of magnitude as V_{in} . Bridge excitation was set at 3 volts and with the gain of the conditioning card set at 20, the output saturated the circuit, rated at ± 10 volts.

Failure Modes

All beams tested to failure, Beams 1,4 and 5 showed massive amounts of shear web damage (Figs. 42-44). Tension flanges of Beams 1 and 4 released from the C-channel flanges at the adhesive joint. Visible damage on both these beams runs from the tip of the shear stiffener at the end of the beam from which the outer flange released, along the fillet of the tension side C-channel flange. Beam 5 (static test) shows a more symmetric pattern of damage, "flowing" from the end of a stiffener up and along the fillet, down past the opposite stiffener tip and back along the bottom

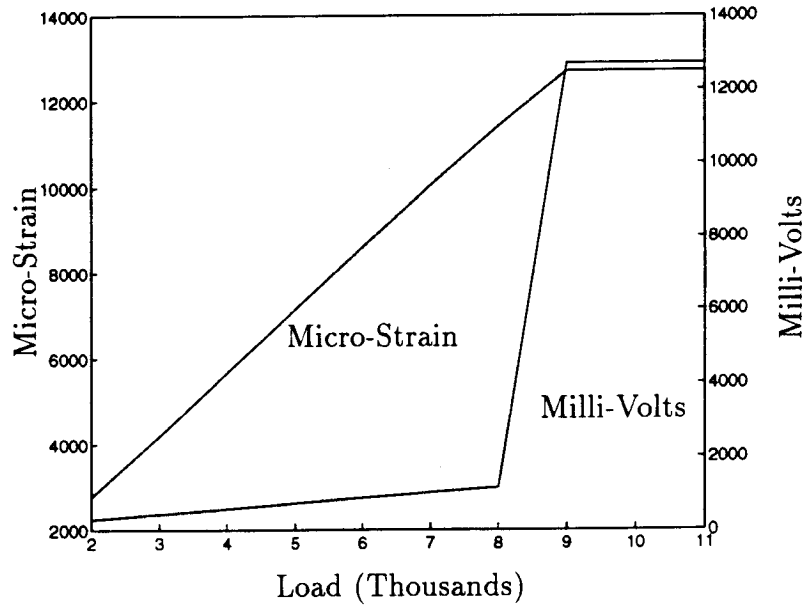


Figure 41. Micro Strain and milli-volt response to strain gage failure.

fillet. The compression zone in the compression flange of Beam 5 (Fig. 44) is similar in appearance to that of a compression failure of a coupon (Fig. 45).

Failure of Beam 5 was recorded using VHS video cassette equipment. Examination of the failure process does not clearly establish failure mode, i.e., compression flange failure precipitating shear web failure or vice versa. To attempt to clarify the failure sequence, a volume of the shear web, immediately center of the tip of the shear stiffener (approximately $1 \times 2.3 \times 0.06$ inches) was modeled with 0, 50 and 90 percent reductions in elastic constant values. The results of the FEA (Fig. 46) describe an increasing x component of compressive stress in the compression flange, at the site of failure in Beam 5, as the degree of web damage is increased. It is the author's opinion that shear web failure precipitated the compression failure in the flange of Beam 5.

It is hypothesized that shear web failure preceded tension flange adhesive failure in Beams 1 and 4 as well. Examination of both beams (Fig. 42-43) reveals a knee on the tension side of the beam, directly in front of the shear web stiffener. Localized failure of the web would effectively produce a joint in the beam. The joint could

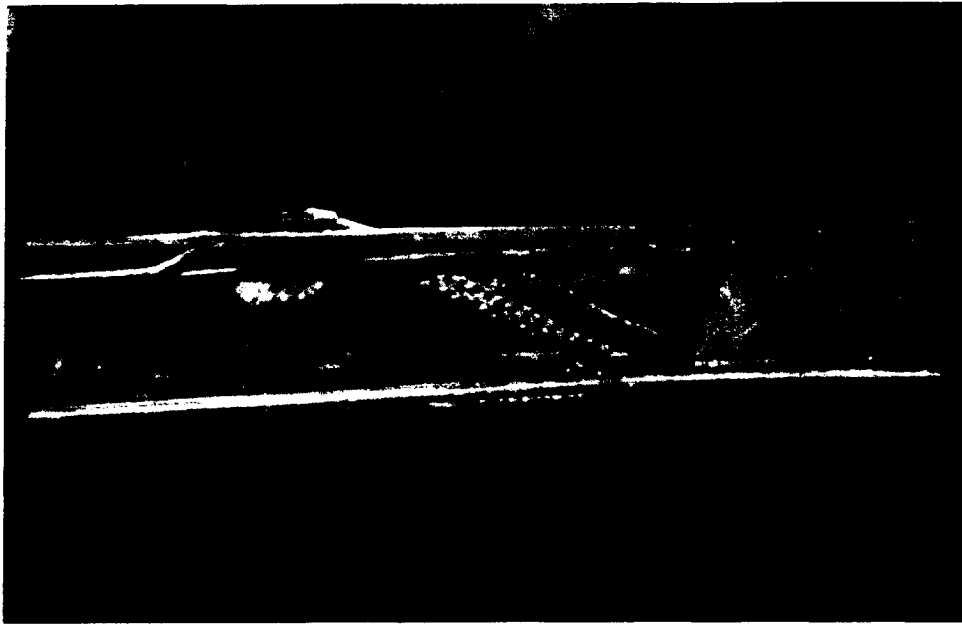


Figure 42. Failure of Beam 1.

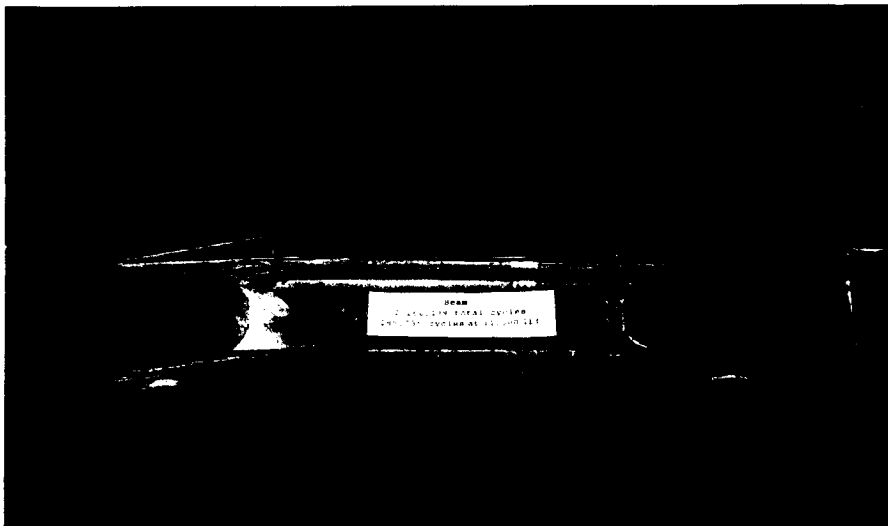


Figure 43. Failure of Beam 4.

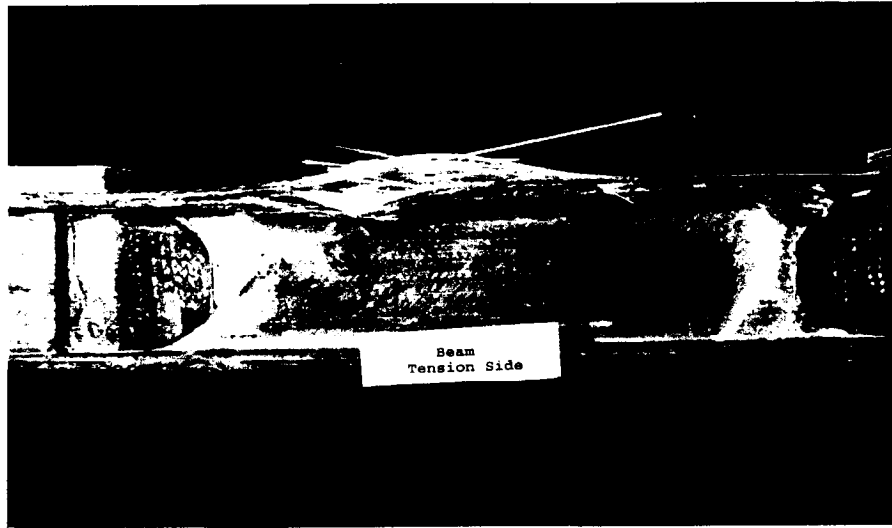


Figure 44. Failure of Beam 5.

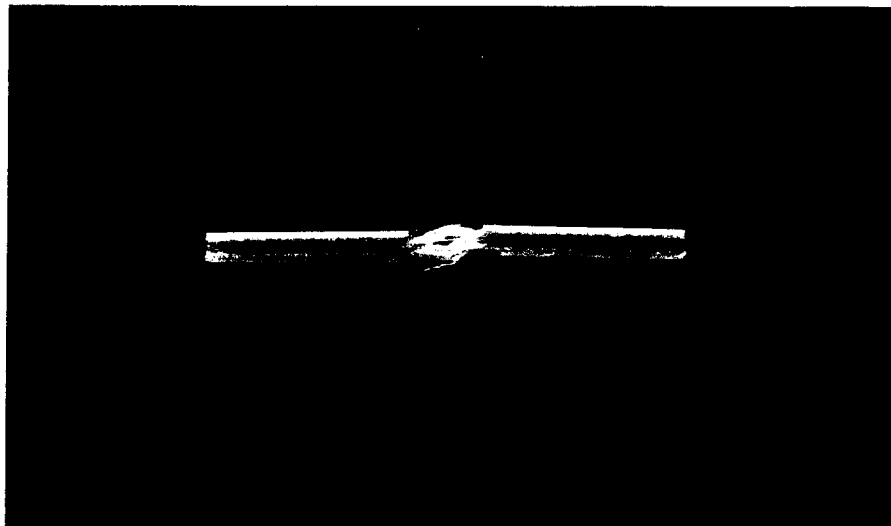


Figure 45. Compression failure of flange 1 coupon.

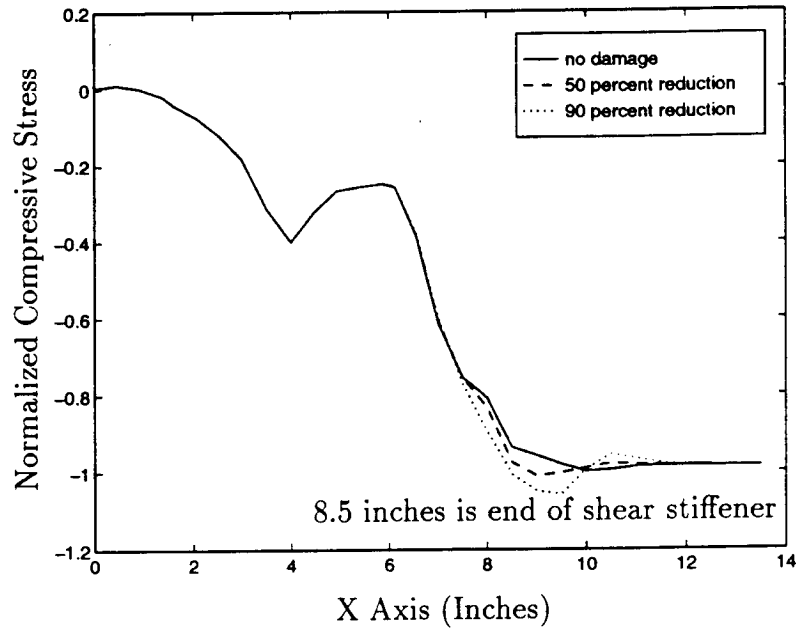


Figure 46. Normalized flange compressive stress with damage in shear web.

cause local adhesive failure at the flange interface due to compressive stress and a shedding of shear stress from the web to the flange. This damage zone would then be a nucleation site for crack growth in the adhesive layer due to shear.

Coupon Correlation

While flange 1 and 2 are not identical materials (Table 4), a comparison of fatigue data, flange 1 material tested in coupon geometry and flange 2 tested as part of Beam 4, does have guarded merit. A few explanatory comments about Figs. 47-48 are in order. Gage section breaks were not obtained from tension specimens from flange 1 material, i.e., the coupon data points in Fig. 47 are failures at the tabs, as a result of stress concentrations, as opposed to material failure in the gage section. This is a well known problem in fatigue testing of composite materials comprised of a high percentage of 0° fibers [15]. All coupon specimens tested in compression fatigue broke in the gage section, except the one specimen that did not break. This data point and

all beam data points that do not coincide with failure of the beam are marked with arrows, indicating run-outs. As a result of a compression flange failure on Beam 4 all tension data points for this beam are marked with arrows. All beam data points are plotted as strain level vs number of cycles at that strain, not cumulative cycles (Table 12, sequence column).

The 10 and 8 percent decade lines found on the tension and compression graphs respectively are based on empirical findings, used extensively in the literature [8],[7],[15] and are plotted using the equation

$$\epsilon = \epsilon_{uts} - b * \log(N).$$

ϵ_{uts} is the strain at failure of the material, b is the slope of the curve and N is the number of fatigue cycles¹. Table 21 lists the strain at failure for the flange 1 coupons and the compression flange of Beam 5. Coupon compressive and tensile ϵ_{uts} were determined from the average value of three static tests in compression and four in tension. ϵ_{uts} for the compression flange of Beam 5 was derived from a least squares data fit (previously described in Chapter 2) of data taken from Fig. 40, using the load range of 0 to 9,000 lbf.

	$\mu\epsilon_{uts}$
Coupon	
Tension	22,386
Compression	14,466
Beam Flange	
Compression	19,180

Table 21. Micro-strain at failure for coupons made from flange 1 material and the compression flange of Beam 5. All geometries were tested in a static ramp loading regime.

While the tension data is of extremely limited value (Fig. 47), due to the failure

¹This equation is usually expressed in terms of stress. Micro-strain was used in this thesis to permit a direct comparison of experimental results.

modes of the coupons, the compression data (Fig. 48) allows for tractable conclusions. First, it is interesting to note the correlation between the 8 percent per decade decay line and the data set, especially the coupon data set. The compression data seems to support previous findings [16], that composite coupon data is conservative relative to material structural response. Note that the compressive strain at failure for the beam is approximately 30% greater than that of the corresponding value for the coupons. The compression flange of Beam 4 failed after 290,000 cycles at $9000 \mu\epsilon$. The only coupon specimen to exceed this life in cycles was tested at approximately $6500 \mu\epsilon$ (the coupon that did not break). Furthermore, consider that the beam had experienced approximately 2 million cycles at lower micro-strain levels, i.e., the beam data is presented in a manner that neglects the previous fatigue history of the beam.

However, the coupon compression strain to failure may be reduced in this case due to the configuration with the $\pm 45^\circ$ layers on the outside, as indicated in current research by D. Samborsky at MSU. Thus, the coupon S-N data might require shifting upward by as much as 20% in $\mu\epsilon$ to reflect testing problems in compression with a short gage section and $\pm 45^\circ$ layers on the outside. This would put the coupon and flange data in better agreement.

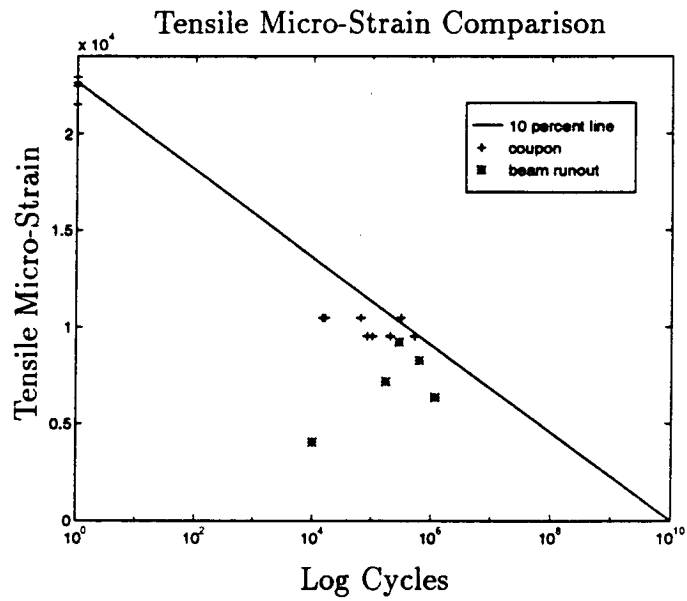


Figure 47. Comparison of flange 1 tensile coupon results with Beam 4.

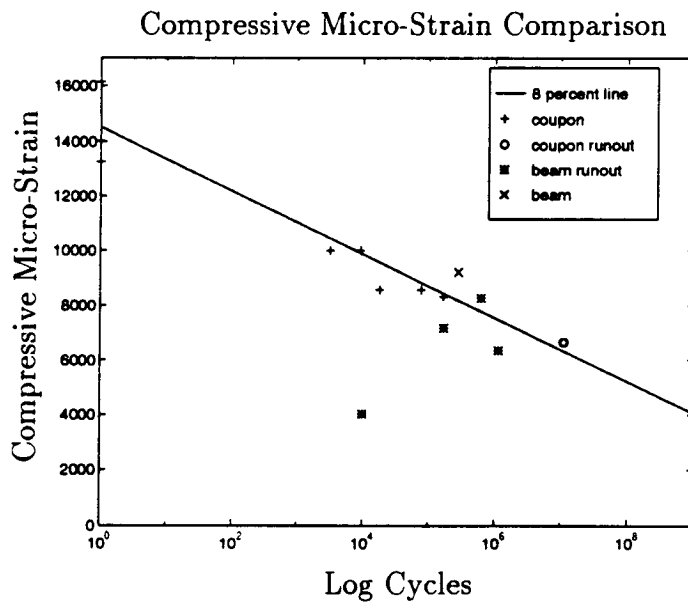


Figure 48. Comparison of flange 1 compressive coupon results with Beam 4.

CHAPTER 5

CONCLUSIONS

The primary purpose of this research was to develop a substructure representative of a wind turbine blade, as well as an apparatus for testing and test procedures that would allow fatigue testing in the laboratory at a minimum frequency of 5 Hz. Beam 4, tested in fatigue, and Beam 5, tested statically, clearly demonstrate the capabilities of testing the beam flange material to the failure range, despite hypothesized shear web failure as the initiation mechanism for beam failure. Beam 4 completed over 2 million stress cycles (285,735 of which were at approximately $9000 \mu\epsilon$), surpassing the coupon performance of similar material, and Beam 5 experienced a definite compression flange failure at a strain consistent with coupon data.

The addition of ply-drops in the flanges of Beams 3-5, with the original intention of forcing flange failure into the gage section, drew attention to the problem inherent in ply-drops, that of delamination. This is significant in that ply-drops are commonly used in composite structures where the laminate changes thickness. This thesis brings a new focus to the ply drop problem, as delamination was experienced even for single ply drops, while industry may drop two or three plies at once.

Other damage development in the beam was largely predictable from coupon results. First ply cracking was in the ± 45 layers, with the tension flange off-axis plies showing accelerated crack growth relative to the compression flange. The longitudinal cracks that developed in the 0° material of both flanges of Beams 4 and 5 are hypothesized to be a result of transverse strain and the constraint of the off-axis plies.

The sudden change in stiffness of Beam 4, near the end of its lifetime, corresponds with investigations of stiffness change conducted on coupons dominated by 0° fibers.

The ANSYS finite element Solid45 provided accurate results with minimum computer storage space and solution time relative to elements with higher order shape functions or those with 20 as opposed to 8 nodes (both requiring more computer memory and time). The 3-dimensional aspects of Solid45 allowed for exact geometric modeling of the beam and detailed description of the strain/stress fields. The FEA solution of the stress field in the adhesive layer of the flanges supported the design change to Configuration 3.

The close correlation between beam theory, FEA and experimental micro-strain results confirms that despite the low l/d ratio of the beam and the use of average orthotropic material properties, the stress/strain and displacement solutions are those of a beam—a hybrid structural component was not developed. While beam theory displacement results did differ more than the FEA displacement solution from experimental results, the error present in the values of the material elastic constants may well account for this discrepancy. Due to the discrete nature of the finite element method this error would be minimized relative to the beam theory.

Recommendations

The hypothesized shear web failure of Beams 4 and 5 may be eliminated by an increase in thickness of the web. Adding a third layer of $\pm 45^\circ$'s in the lay-up of the C-channel, while maintaining a v_f value of at least 40 percent, is recommended.

The next procedural step in this direction of research is to begin a methodical testing and comparison of material in both coupon geometry and as flange material. If the conservative nature of coupon results can be verified and quantified, the high

frequency test methodologies developed in previous research would quickly establish baseline fatigue data useful to the rotor blade design engineer.

This research has highlighted the significance of structural detail in the failure modes of a structure, as flange failure was the last mode of failure to be achieved. The relatively high levels of strain/stress (over 2.2 million cycles at or above $6000 \mu\epsilon$) at which a small structure is able to operate has also been demonstrated. Employing the analytical and modeling capabilities of 3-dimensional finite elements to design components would clarify the design process which in turn would likely result in a reduction of both weight and premature failures of wind turbine blades.

There are presently several non-destructive evaluation techniques, e.g. acoustic emission, stiffness degradation and modal analysis, being pursued in the attempt to predict in-service failures of composite structures. The beam developed in this research provides a laboratory based structure which would be ideal for the testing of these techniques.

Delaminations originating at the sites of ply-drops, an unresolved issue in this research, call for further investigation. Delaminations were detected in Beam 4 after only 10,000 cycles at approximately $6000 \mu\epsilon$. The chronic nature of the delaminations in both Beams 3 and 4 indicate that this type of initiation process for delaminations could be a significant problem in composite structures employing ply-drops, which certainly includes the vast majority of composite wind turbine blades. The ply drop problem in current rotor blades may be shielded by even more severe structural design limitations, which prevent blade strain levels (even in blade testing) from approaching those investigated in this thesis.

REFERENCES CITED

- [1] D. A. Spera, ed., *Wind Turbine Technology*. New York, New York: ASME Press, 1994.
- [2] P. E. Hemke, *Elementary Applied Aerodynamics*. New York, New York: Prentice-Hall, Inc., 1946.
- [3] B. George, "Reaping the Wind," *American Heritage of Invention & Technology*, vol. 8, pp. 8–15, Winter 1993.
- [4] National Renewable Energy Laboratory, *Wind Energy Program Overview*, 1993.
- [5] Committee on Assessment of Research Needs for Wind Turbine Rotor Materials Technology, "Assessment of Research Needs for Wind Turbine Rotor Materials Technology," tech. rep., National Research Council, Washington, D.C., 1991.
- [6] R. M. Reed, "Long Term Fatigue of Glass Fiber Reinforced Composite Materials for Wind Turbine Blades," Master's thesis, Montana State University, Bozeman, MT 59717, October 1991.
- [7] R. F. Creed, "High Cycle Tensile Fatigue of Unidirectional Fiberglass Composite Tested at High Frequency," Master's thesis, Montana State University, Bozeman, MT 59717, October 1993.
- [8] A. J. Belinky, "High Cycle Compressive Fatigue of Unidirectional Glass/Polyester Performed at High Frequency," Master's thesis, Montana State University, Bozeman, MT 59717, October 1994.
- [9] P. Kurath and D. Socie, "The Relationship Between Observed Fatigue Damage and Life Estimation Models," tech. rep., Lewis Research Center, NASA, 1988.
- [10] J. E. Shigley and C. R. Mischke, *Mechanical Engineering Design*. New York, New York: McGraw-Hill Book Company, 1989.
- [11] J. Bannantine, J. Comer, and J. Handrock, *Fundamentals of Metal Fatigue Analysis*. Englewood Cliffs, New Jersey: Prentice Hall, 1990.
- [12] D. Broek, *Elementary Engineering Fracture Mechanics*, ch. 10, p. 261. Boston: Kluwer Academic Publishers, 1986.
- [13] K. L. Reifsnider, *Fatigue of Composite Materials*, pp. 17–26. New York, New York: Elsevier, 1991.
- [14] K. Garrett and J. Bailey, "Multiple transverse fracture in 90° cross-ply laminates of a glass fibre-reinforced polyester," *Journal of Materials Science*, vol. 12, pp. 157–168, January 1977.
- [15] J. F. Mandell, *Developments in Reinforced Plastics -2*, ch. 4, pp. 67–107. New York, New York: Applied Science Publishers, 1982. Edited by G. Pritchard.

- [16] Committee on Life Prediction Methodologies for Composite Materials, "Life Prediction Methodologies for Composite Materials," tech. rep., National Materials Advisory Board, Washington, D.C., 1991.
- [17] P. K. Mallick, *Fiber-Reinforced Composites*. New York, New York: Marcel Dekker, Inc., 1988.
- [18] J. M. Gere and S. Timoshenko, *Mechanics of Materials*. Boston, Massachusetts: PWS Engineering, 1984.
- [19] R. Cook and W. Young, *Advanced Mechanics of Materials*, ch. 1, p. 7. New York: Macmillan Publishing Company, 1985.
- [20] I. American Institute of Steel Construction, ed., *Load & Resistance Factor Design*, ch. K, p. 79. American Institute of Steel Construction, Inc., 1986.
- [21] C. W. Hedley, "Mold Filling Parameters in Resing Transfer Molding of Composites," Master's thesis, Montana State University, Bozeman, MT 59717, April 1994.
- [22] J. M. Gere and S. Timoshenko, *Mechanics of Materials*, ch. 7, p. 354. Boston, Massachusetts: PWS Engineering, 1984.
- [23] J. M. Gere and S. Timoshenko, *Mechanics of Materials*, ch. 7, p. 408. Boston, Massachusetts: PWS Engineering, 1984.
- [24] J. M. Gere and S. Timoshenko, *Mechanics of Materials*, ch. 5, p. 208. Boston, Massachusetts: PWS Engineering, 1984.
- [25] A. Highsmith and K. L. Reifsnider, *Damage in Composite Materials*, p. 104. Philadelphia, Pa.: ASTM, 1980.
- [26] P. Lagace, "Nonlinear stress-strain behavior of graphite/epoxy laminates," *AIAA Journal*, vol. 23, no. 10, pp. 1583-1589, 1985.
- [27] S. Amijima, "Nonlinear stress-strain response of laminated composites," *Journal of Composite Materials*, vol. 13, pp. 207-218, July 1979.
- [28] J. M. Gere and S. Timoshenko, *Mechanics of Materials*, ch. 7, pp. 414-418. Boston, Massachusetts: PWS Engineering, 1984.

APPENDICES

APPENDIX A

Mold Design

Two resin transfer molds (RTM) were manufactured for this research. Tempered glass was used in both instances to allow for visual inspection during the injection process.

The concept of Hedley's flat mold [21] was enlarged to produce a composite sheet 33.6 inches by 9 inches by 0.17 inches thick. A square 0.5 inch by 0.5 inch gasket was used to both seal the mold and provide the desired thickness. Injection sites were located in the center of the mold to reduce flow distance of the resin, both ends were vented, (Figs. 49).

The c-channel mold consisted of a male and female component and a top sheet of 0.375 inch tempered glass. The male and female parts were aligned with fixed dowels in the base of the bottom plate and sealed with a 0.125 inch thick piece of flat neoprene. The top sheet was sealed using an 0.125 inch O-ring, (Figs. 50).

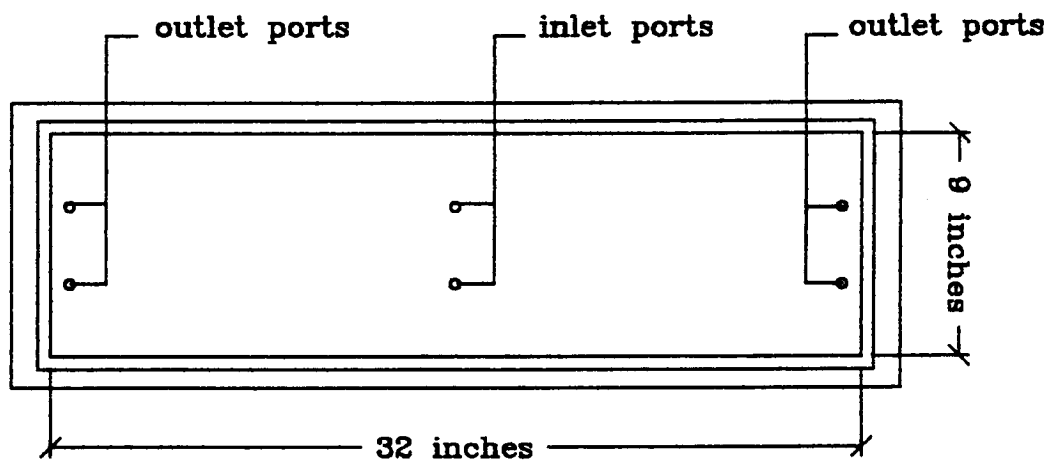
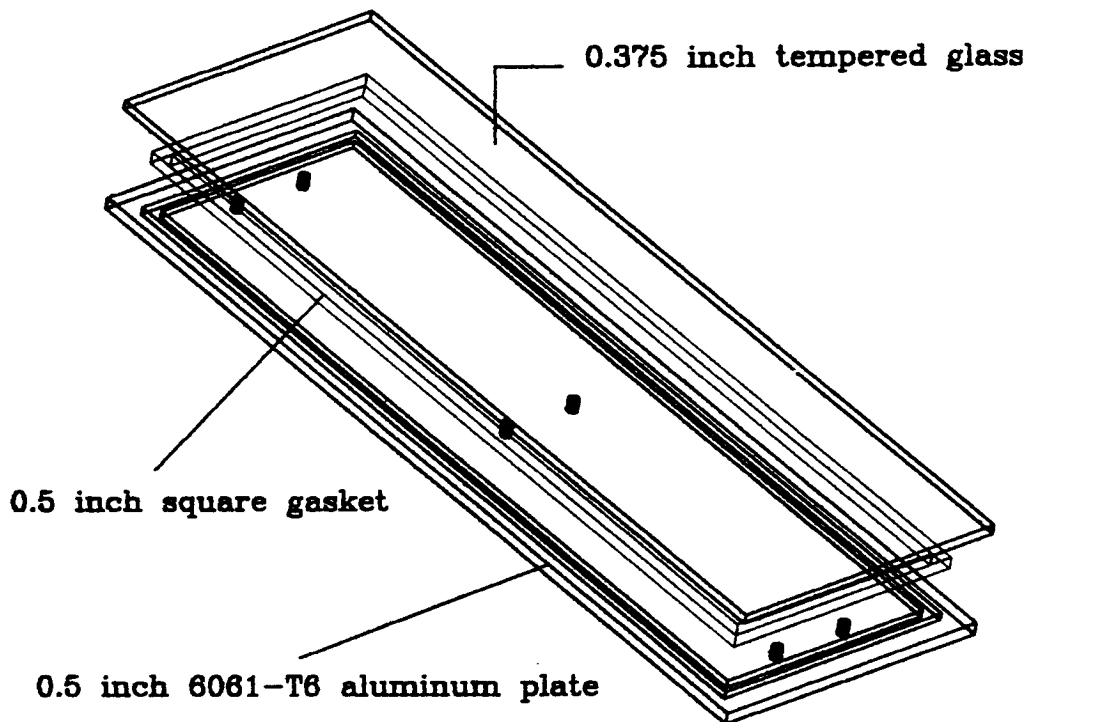


Figure 49: Three dimensional and plan view of flate plate mold.

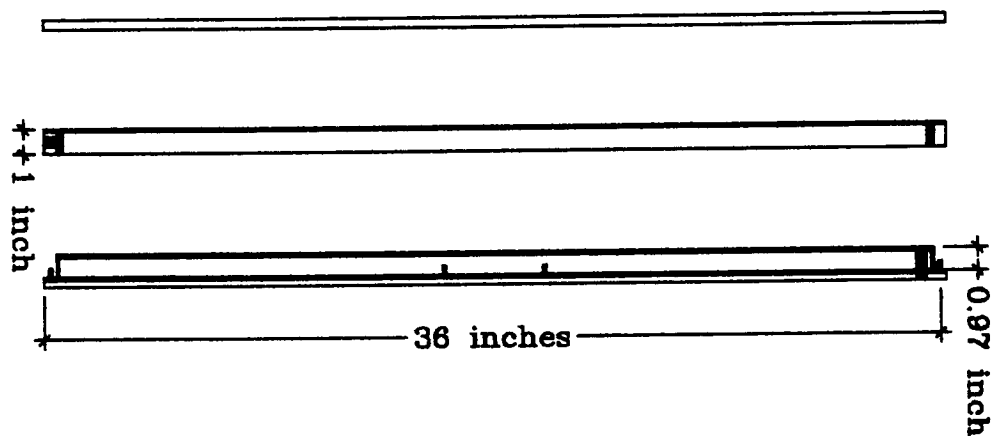
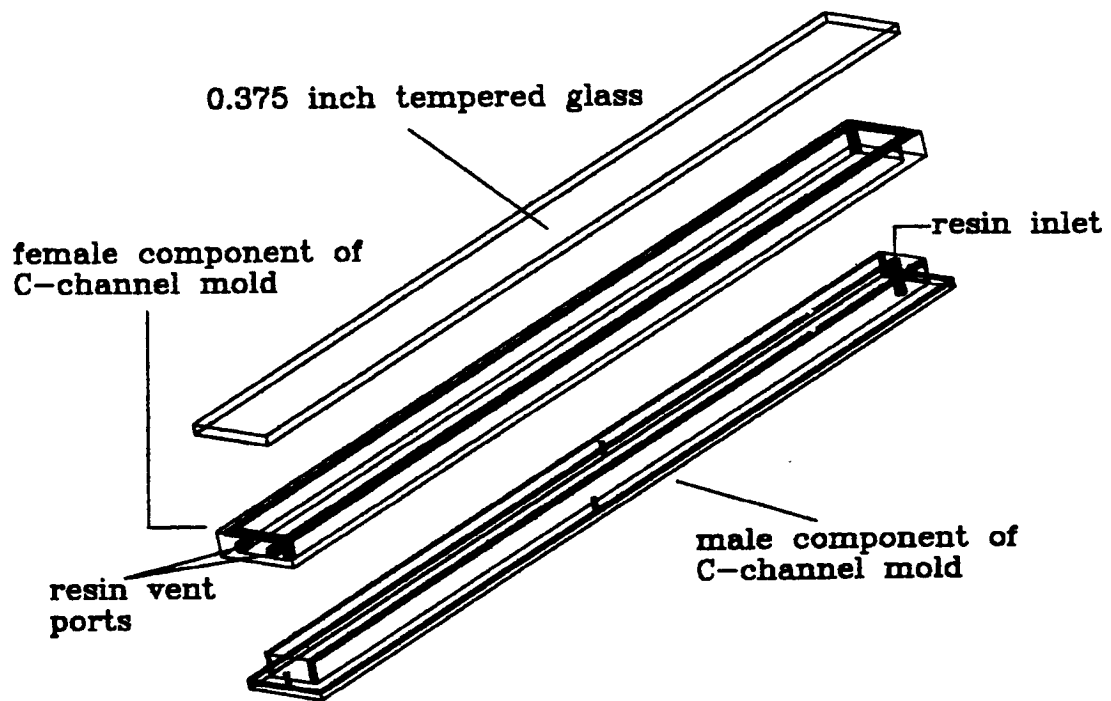


Figure 50: Three dimensional and side view of C-channel mold.

APPENDIX B

Test Fixture

The ideal test fixture would be infinitely stiff, transferring all applied loads to the test specimen. A simply supported beam test is commonly configured so that the outside supports are contacting a solid floor mass and the load is delivered over-head. The MTS load frame configuration presented conceptual as well as safety considerations in the design process.

As previously mentioned, fatigue tests were to be conducted using an R value of 10. In order to control the test in load control, the most straight-forward means of conducting the test, the fixture must be connected to the load cell of the MTS. The load cell is mounted overhead and the actuator/piston delivers the load from below, figure(51).

Due to the size of the outside support component of the test fixture it was attached to the load cell, eliminating any movement of this piece. To maintain balanced four-point loading and to eliminate the transfer of a bending moment to the load frame a pinned joint was included in the design. Neither the actuator shaft nor the connecting pin for the load cell are designed to withstand significant loading via bending moment. This joint was placed in the load component, attached to the bottom grip.

Both components of the fixture were sized to limit their deflections to .001 inch at 50,000 lbf, the load capacity of the frame. A factor of safety of 2 was used throughout the design process.

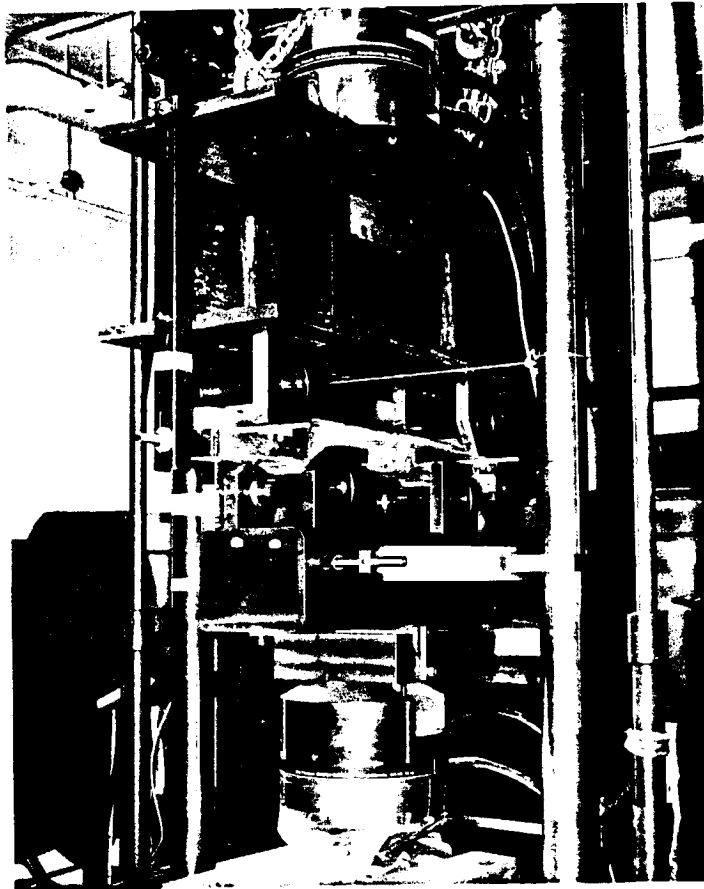


Figure 51. Load fixture mounted in MTS load frame with composite beam in place.